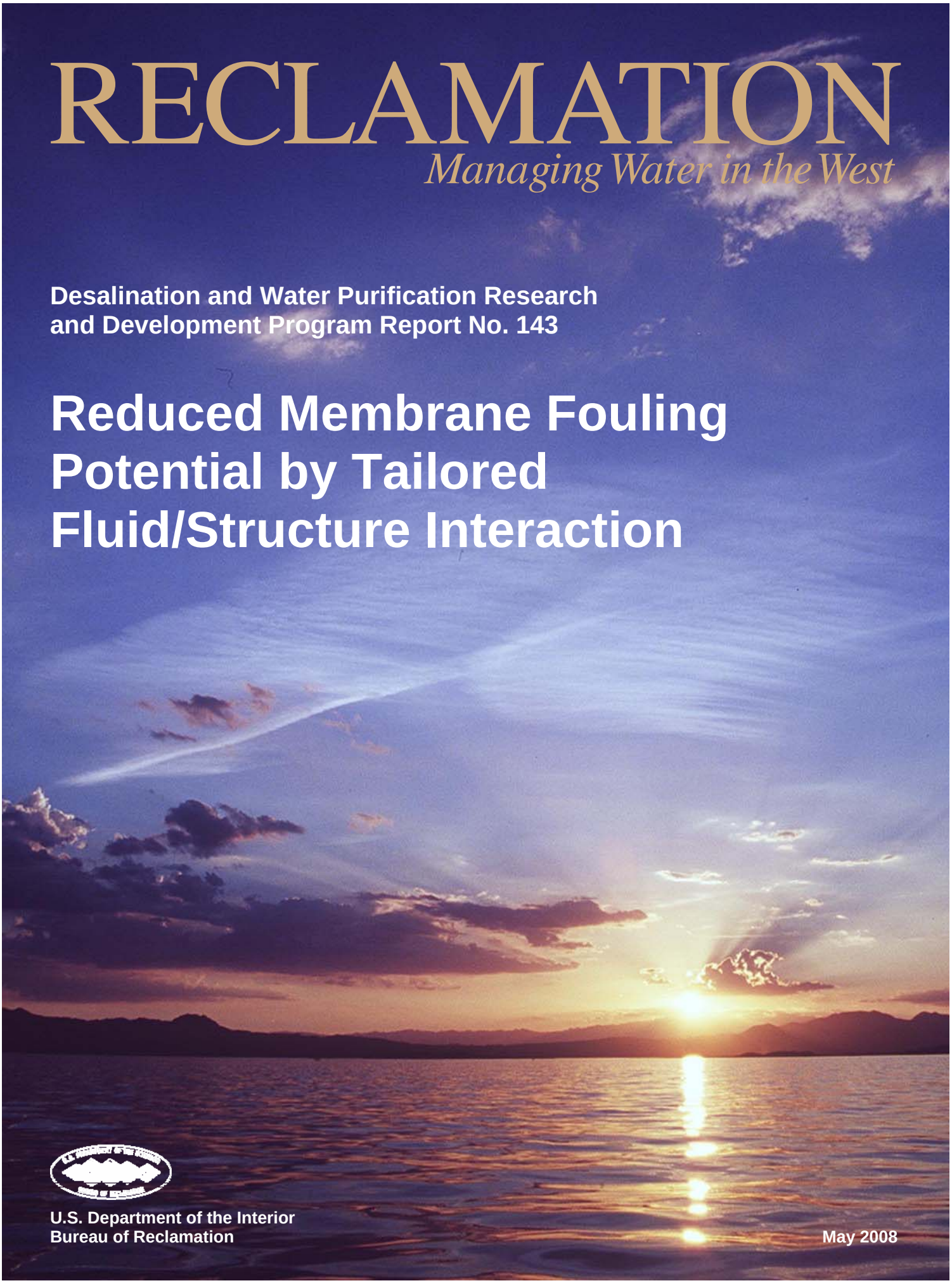

RECLAMATION

Managing Water in the West

Desalination and Water Purification Research and Development Program Report No. 143

Reduced Membrane Fouling Potential by Tailored Fluid/Structure Interaction

U.S. Department of the Interior
Bureau of Reclamation

May 2008

REPORT DOCUMENTATION PAGE

Form Approved
OMB No. 0704-0188

1. REPORT DATE *(DD-MM-YYYY)*	2. REPORT TYPE	3. DATES COVERED *(From - To)*
May 2008	Final	October 2005 to June 2007

4. TITLE AND SUBTITLE
Reduced Membrane Fouling Potential by Tailored Fluid/Structure Interaction

5a. CONTRACT NUMBER
Agreement No. 05-FC-81-1155

5b. GRANT NUMBER

5c. PROGRAM ELEMENT NUMBER

6. AUTHOR(S)
Kevin J. Farrell

5d. PROJECT NUMBER

5e. TASK NUMBER
Task A

5f. WORK UNIT NUMBER

7. PERFORMING ORGANIZATION NAME(S) AND ADDRESS(ES)
Heat Transfer Research, Inc.
150 Venture Drive
College Station, Texas 77845

8. PERFORMING ORGANIZATION REPORT NUMBER

9. SPONSORING / MONITORING AGENCY NAME(S) AND ADDRESS(ES)
U.S. Department of the Interior
Bureau of Reclamation,
Denver Federal Center
PO Box 25007, Denver CO 80225-0007

10. SPONSOR/MONITOR'S ACRONYM(S)

11. SPONSOR/MONITOR'S REPORT NUMBER(S)
DWPR Report No. 143

12. DISTRIBUTION / AVAILABILITY STATEMENT
Available from the National Technical Information Service
Operations Division, 5285 Port Royal Road, Springfield VA 22161

13. SUPPLEMENTARY NOTES
Report can be downloaded from Reclamation Web site:
www.usbr.gov/pmts/water/publications/reports.html

14. ABSTRACT ***(Maximum 200 words)***

Vibratory elements within the feed spacer of a spiral-wound element can be beneficial to reduce the membrane fouling potential and can disrupt the concentration polarization layer. The desired result is longer life for the membrane and increased permeate flux and purity. Using the feed spacer geometry of a commercially available spiral-wound reverse osmosis cartridge, we used computational fluid dynamics (CFD) to assess what change in the surface shear stress and concentration could be effected by the incorporation of a dynamic element within the current feed spacer design. The simulation results from several designs showed that a cantilevered ribbon with a fluttering motion caused an increase in the salt concentration and surface shear stress of 1 percent and 25 percent, respectively. Further promotion of the concept requires investigation of the fluid-structure response via coupled CFD/finite element structural analysis and then a confirmatory experiment.

15. SUBJECT TERMS
selenium, reverse osmosis, calcium sulfate, electrodialysis metathesis, calcium chloride, sodium sulfate, sodium cloride, zero-discharge desalination process, supernatant

16. SECURITY CLASSIFICATION OF:			17. LIMITATION OF ABSTRACT	18. NUMBER OF PAGES	19a. NAME OF RESPONSIBLE PERSON
a. REPORT	b. ABSTRACT	c. THIS PAGE	SAR	61	Saied Delagah
UL	UL	UL			19b. TELEPHONE NUMBER *(include area code)* 303-445-2248

Desalination and Water Purification Research and Development Program Report No. 143

Reduced Membrane Fouling Potential by Tailored Fluid/Structure Interaction

Prepared for Reclamation Under Agreement No. 05-FC-81-1155 Task A

by

Heat Transfer Research, Inc.

U.S. Department of the Interior
Bureau of Reclamation
Technical Service Center
Water and Environmental Services Division
Water Treatment Engineering Research Team
Denver, Colorado

May 2008

MISSION STATEMENTS

The mission of the Department of the Interior is to protect and provide access to our Nation's natural and cultural heritage and honor our trust responsibilities to Indian tribes and our commitments to island communities.

The mission of the Bureau of Reclamation is to manage, develop, and protect water and related resources in an environmentally and economically sound manner in the interest of the American public.

Disclaimer

The views, analysis, recommendations, and conclusions in this report are those of the authors and do not represent official or unofficial policies or opinions of the United States Government, and the United States takes no position with regard to any findings, conclusions, or recommendations made. As such, mention of trade names or commercial products does not constitute their endorsement by the United States Government.

Acknowledgement

The research described herein was sponsored in part by the Desalination and Water Purification Research and Development Program, Bureau of Reclamation, U.S. Department of the Interior, Agreement No. 05-FC-81-1155.

Acronyms

CFD	computational fluid dynamics
ED	electrodialysis
ft^2	square foot
ft^3	cubic foot
gal/day	gallons per day
gal/min	gallons per minute
in	inch
in^2	square inch
in^3	cubic inch
kPag	kilopascal gauge
L/min	liters per minute
L/s	liter per second
m	meter
m^2	square meter
MF	microfiltration
mgd	million gallons per day
mg/L	milligrams per liter
mm	millimeter
mm^2	square millimeter
mm^3	cubic millimeter
MPa	megapascal
NaCl	sodium chloride
NF	nanofiltration
ppm	parts per million
psi	pounds per square inch
psig	pounds per square inch gauge
RANS	Reynolds-averaged Navier-Stokes
RNG	renormalized group
Reclamation	Bureau of Reclamation
RO	reverse osmosis
SW	spiral-wound
SWRO	seawater reverse osmosis

Acronyms (continued)

UF	ultrafiltration
%	percent
°C	degrees Celsius
°F	degrees Fahrenheit
µg/L	micrograms per liter
µm	micrometer
µS/cm	microsiemens per centimeter

Nomenclature

A'	Constant	—
B'	Constant	—
c	Concentration, mass of solute per unit mass of solution	—
c'	Fluctuating concentration	—
C_f	Skin friction coefficient	—
c_{in}	Concentration at inlet	—
C_L	Lift coefficient	—
c_ℓ	Chord length	m
c_{out}	Concentration at outlet	—
C_μ	Constant in eddy viscosity relation	—
$\mathrm{C}(a_r)$	Theodorsen aerodynamic response function	—
D	Mass diffusivity	m^2/s
d	Span length	m
d_h	Hydraulic diameter for spacer-filled channel	m
D_t	Turbulent diffusivity	m^2/s
E	Flexural modulus	Pa
f	Frequency	Hz
f	Friction factor	—
f_R	Frequency ratio	—
F_x	Specific body force in x-direction	m/s^2
F_y	Specific body force in y-direction	m/s^2
F_z	Specific body force in z-direction	m/s^2
h_{ch}	Height of channel	m
I	Second moment of area	m^4
i	Imaginary unit number, $\sqrt{-1}$	—
I_b	Second moment of area per unit width	m^3
J_0	Bessel function of first kind, zero order	—
J_1	Bessel function of first kind, first order	—

Nomenclature (continued)

k	Stiffness	N/m
L	Length of channel	m
$\tilde{L}$	Unsteady lift per unit span	N/m
ℓ	Characteristic length	m
m	Mass per unit cross-sectional area	kg/m^2
n	Exponent	—
p	Pressure	Pa
Re_{ch}	Reynolds number based on channel height	—
Re_{Dh}	Reynolds number based on hydraulic diameter	—
S_{slit}	Surface area of empty channel	m^2
S_{sp}	Surface area of filaments	m^2
S_{vsp}	Surface area of filaments over volume of filaments	m^{-1}
$\mathrm{S}(\alpha_r)$	Sears aerodynamic response function	—
Sc_t	Schmidt number for turbulent flow, i.e., ratio of turbulent momentum diffusivity to turbulent mass diffusivity	—
T	Period	s
t	Time	s
T_e	Tension	N
u	Velocity; velocity in x-direction	m/s
u'	Fluctuating velocity in x-direction	m/s
u_{ave}	Average through-flow velocity in spacer-filled channel	m/s
v	Velocity in y-direction	m/s
v'	Fluctuating velocity in y-direction	m/s
$\tilde{v}$	Disturbance velocity	m/s
V	Velocity	m/s
$V_{critical}$	Critical velocity for onset of galloping or flutter	m/s
V_s	Flutter speed	m/s
V_{sp}	Volume of filaments	m^3
V_{tot}	Volume of channel without feed spacer	m^3
w	Velocity in z-direction	m/s
w'	Fluctuating velocity in z-direction	m/s

Nomenclature (continued)

W_e	Mass per unit length	kg/m
X, Y, Z	Cartesian coordinates	m
x, y, z	Cartesian coordinates	m
Y_0	Bessel function of second kind, zero order	—
Y_1	Bessel function of second kind, first order	—

Greek

α	Angle-of-attack	rad
β	Flutter limit stiffness parameter	—
Δp_{ch}	Pressure drop in channel	Pa
ϵ	Normalized twist angle function	—
ε	Voidage of spacer channel	—
ε_t	Turbulence dissipation rate	m^2/s^3
κ	Turbulence kinetic energy	m^2/s^2
λ_1	Constant used for fundamental frequency and mode shape for cantilevered beam	—
μ	Dynamic viscosity	kg/m s
ϕ_1	Mode shape function	—
ψ_1	Displacement function	—
φ_s	Phase angle of Sears function	rad
ν	Kinematic viscosity	m^2/s
ν_t	Eddy viscosity, turbulent viscosity	m^2/s
ρ	Density	kg/m^3
σ_1	Constant used for fundamental mode shape for cantilevered beam	—
τ	Shear stress	Pa
τ_{xx}	Viscous fluid element stress acting in *x*-direction on face with *x*-direction normal	Pa
τ_{xy}	Viscous fluid element stress acting in *x*-direction on face with *y*-direction normal	Pa
τ_{xz}	Viscous fluid element stress acting in *x*-direction on face with *z*-direction normal	Pa

Nomenclature (continued)

Greek (continued)

τ_{yx}	Viscous fluid element stress acting in *y*-direction on face with *x*-direction normal	Pa
τ_{yy}	Viscous fluid element stress acting in *y*-direction on face with *y*-direction normal	Pa
τ_{yz}	Viscous fluid element stress acting in *y*-direction on face with *z*-direction normal	Pa
τ_{zx}	Viscous fluid element stress acting in *z*-direction on face with *x*-direction normal	Pa
τ_{zy}	Viscous fluid element stress acting in *z*-direction on face with *y*-direction normal	Pa
τ_{zz}	Viscous fluid element stress acting in *z*-direction on face with *z*-direction normal	Pa
ω	Frequency (angular)	rad/s
ω_1	Fundamental natural frequency	rad/s
ω_r	Reduced frequency	—

Other operators

$\overline{qr}$	Time-averaged value of product of q and r

Table of Contents

List of Figures

List of Figures (continued)

1. Executive Summary

Fouling is a critical problem that reduces the permeate flux, requires periodic cleanings, and limits the life of spiral-wound reverse osmosis elements. Because of these detrimental effects, fouling may impede the wider application of membrane-based separation processes.

In general, flow-induced forces on structures can be destructive and are, thus, avoided by design. However, useful motion—both amplitude and frequency—can result from tailoring a system's attributes to elicit the desired vibratory response.

We proposed that vibratory elements within the feed spacer could be beneficial to reduce the membrane fouling potential and to disrupt the concentration polarization layer. The desired result is longer life for the membrane and increased permeate flux and purity.

Using the feed spacer geometry of a commercially available spiral-wound reverse osmosis cartridge, we used computational fluid dynamics (CFD) to assess what change in the surface shear stress and concentration could be effected by the incorporation of a dynamic element within the current feed spacer design, with the motion prescribed *a priori*.

Among simulation results from several designs, we found that a cantilevered ribbon with a fluttering motion caused an increase in the salt concentration and surface shear stress of 1 percent and 25 percent, respectively. The crossflow pressure drop increased by up to 57 percent during one oscillation cycle.

Aerodynamic response functions from thin airfoil theory show that the amplitude of the response diminishes with increasing reduced frequency. We estimated the reduced frequency of the cantilevered ribbon by extrapolating results from an experimental study of paper strips fluttering in air. The aerodynamic response functions predict that the actual response will be approximately 30 percent of the quasi-steady response. Our analysis concerns one small repeating element of a feed spacer; the integrated effect points to a marked improvement in the salt concentration, reduced fouling potential, and a reduced pressure drop—due not only to the diminished time response but also to the fact that the dynamic elements will have random phase throughout the cartridge.

Further promotion of the concept requires investigation of the fluid-structure response via coupled CFD/finite element structural analysis or other multiphysics

modeling and then a confirmatory experiment. In parallel, the practicalities of manufacturing a feed spacer having such vibrating elements must be considered.

2. Background

As the demand for quality freshwater increases around the world, utilities are using desalination[1] to produce freshwater from seawater and brackish water and to improve the quality of freshwater supplies. For many process and manufacturing plants, desalination is fast becoming an economically viable option. All desalting processes involve separation of the feedwater into two streams: the desalted product stream and the concentrate. This separation is accomplished primarily by either thermal or membrane process technologies.

Thermal processes—multistage flash, multiple-effect distillation, and vapor compression—involve evaporation of the feedwater and condensation of the ensuing vapor to provide the desalted product stream. These man-made processes are much like the natural water cycle.

In the membrane separation processes, electrodialysis (ED) and reverse osmosis (RO), synthetically produced membranes are used to separate the two streams at ambient temperatures. ED uses electropotential to drive undesirable salt ions across membranes, leaving the desalted product stream behind. In RO, developed in the 1950s primarily under United States Government funding, a semipermeable membrane acts as a barrier to undesirable substances while allowing the product stream to pass through. Other membrane separation processes, in order of decreasing pore size, are microfiltration (MF), ultrafiltration (UF), and nanofiltration (NF). Among these processes, RO uses the smallest pore size. The market for membranes in desalination processes is robust and expanding, and the competition is fierce (Hairston, 2004). Projected demands for clean water will drive the market for crossflow membrane systems and replacements to over $11 billion in 2011 (McIlvaine, 2007).

While a conventional filter uses a porous material to capture solid particles, an RO element uses a semipermeable membrane to separate out molecular-sized particles. Osmotic pressure attempts to equalize the solute concentration by driving solvent from the side with the lower concentration of solute to the other side. By applying pressure greater than the osmotic pressure but in the reverse direction, one can further purify the solvent. Of course, steps must be taken to make sure that the membrane does not become clogged by the impurities pressed against it. By using crossflow filtration as shown in figure 1, the feed flow carries away the concentrate, while the permeate moves perpendicular to the feed flow.

[1] Desalination, desalinization, and desalting are synonymous.

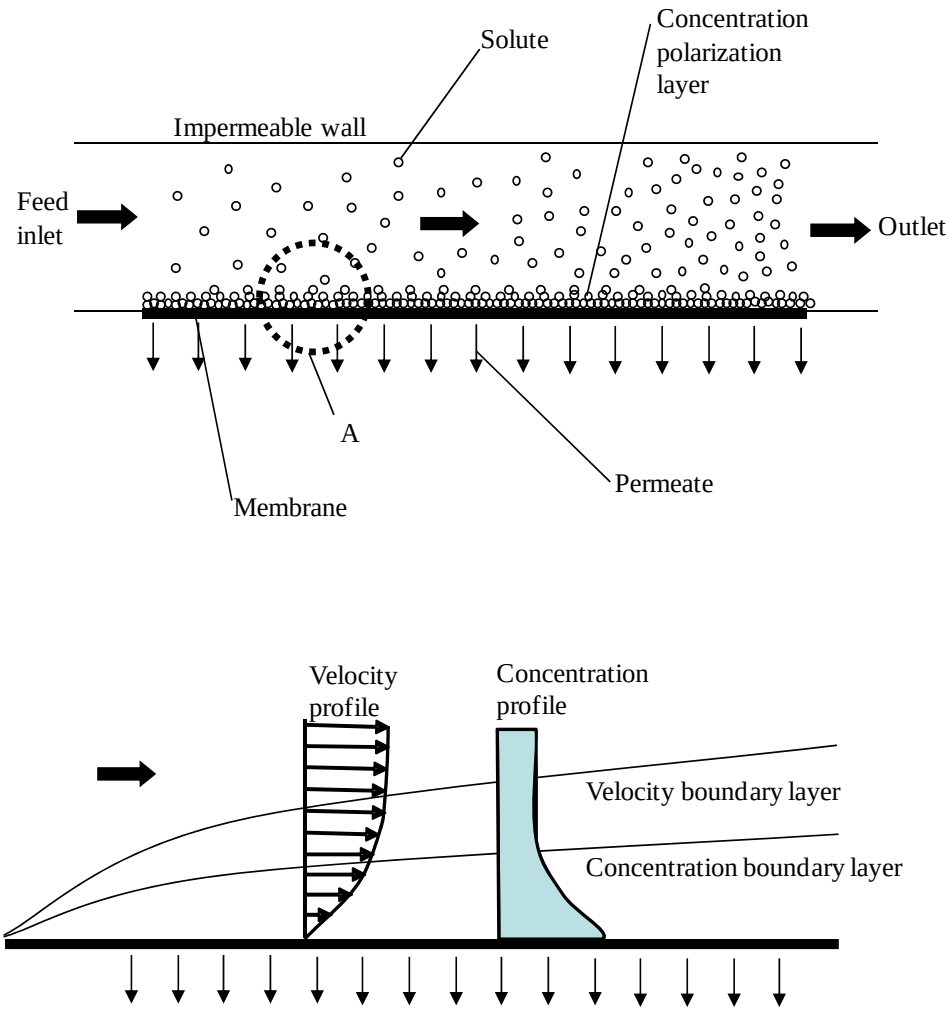

Figure 1. Schematic of crossflow filtration.

The 19th International Desalination Association desalting inventory report (GWI Desal Data, 2006) projected that, as of the end of 2006, considering only units having capacity greater than 26,000 gallons per day, the United States possessed about 16 percent of the worldwide desalting capacity (9.3 billion gallons per day). RO is the principle desalting technology with about 931 RO plants online at the end of 2006 in the United States with a total capacity of approximately 1 billion gallons per day. RO works on many sites because it can tolerate a wide range of total dissolved solids in the feedwater and has a wide range of production capacity. Moreover, it is cost effective, requiring lower capital costs than alternate treatment methods such as evaporation and distillation. Newer membranes are effective at lower pressure than older membranes and also have higher recovery ratios. Worldwide, the installed

capacity of membrane and thermal processes is about equal; however, as older, distillation units go offline, it is probable that the capacity of operating membrane units exceeds that of thermal units (Buros, n.d.).

The percentage of feedwater which permeates the membranes ranges from 30 to 85 percent depending on the level of total dissolved solids (American Water Works Association, 2004). This recovery ratio is limited by the driving pressure and degraded by the formation of scale and fouling. Eventually, when cleaning does not provide acceptable performance, the membrane must be replaced. In 2003, the market for RO membranes was estimated at $145 million per annum (Bureau of Reclamation, 2003).

Particularly when recovery is large, the dissolved salts or ions can become sufficiently concentrated to precipitate on the wetted surfaces of the process components, thereby reducing the quality and quantity of the product stream. Unfortunately, it is difficult to ascertain the exact causes of scale formation or fouling in the RO system; however, several mechanisms can be identified (Barger and Carnahan, 1991):

- Retained particulates and colloids depositing on the membrane
- Salts precipitating near the membrane surface
- Biological growth
- Reaction of feedwater component(s) with the membrane itself
- Large insoluble polymers formed by flocculation on the membrane

Fouling is the most critical problem limiting wider application of membrane-based separation processes (Zhang et al., 2003). Current approaches to predicting and controlling membrane fouling involve pretreating the feedwater and cleaning the membrane. However, complete removal of undesirable substances by pretreatment is not practical or economical. Often, there is little correlation between the feedwater characterization from which the treatment scheme is specified and the actual membrane fouling tendency. A number of performance characteristics can be monitored to initiate a cleaning cycle:

- Decline in flux rates
- Increase in salt passage
- Decline in brine or product flow rates
- Increase in pressure drop

When the permeate flux declines unacceptably (about 15 to 20 percent), a cleaning cycle is initiated, but the restored flux is an ever diminishing fraction of the original flux. Clearly, efforts to remediate the effects of fouling drive a

substantial fraction of capital, operation, and maintenance costs through oversized designs, pretreatment, cleaning, and ultimately membrane replacement. More effective and affordable treatment methods will not only reduce the costs of desalination but also allow feedwater sources of poorer quality to be used.

Steady flow over a bluff or nonstreamlined structure can result in substantial unsteady pressures due to periodic shedding of vorticity in the wake. The correspondence of the frequency and wavelength of the excitation with the natural modes of the structure can elicit a large response. In the time domain, we term this effect *resonance*; in the spatial domain, *coincidence*. The well-known failure of the Tacoma Narrows Bridge was due to the coincidence of a torsional mode and the periodic aerodynamic loads of the prevailing winds. In tubular heat exchangers, fluidelastic instability and vortex shedding can lead to tube failure and accelerated wear rates. However, proper consideration of the excitation force and the structural characteristics during design can minimize or eliminate vibration problems in thermal-hydraulic equipment.

While in most circumstances the fluctuating forces of fluid/structure interaction are undesirable, we suggest introducing high-response features in the mesh spacer structure(s) in proximity to the membranes. The ensuing elevated shear stresses prevent the adhesion of scale and other foulants to the membrane surface and dynamically alter the concentration boundary layer. Vortex generators on aircraft wings serve an analogous function in that they energize the boundary layer at the surface by drawing energy from the freestream and, thereby, delay flow separation and the accompanying drag penalty. By tuning the resonant frequency of certain features of the mesh spacer structure with the frequency of excitation, we can increase the strength of the alternating shear stresses in the wake.

The ability to actively or passively manipulate a flow field to achieve a desired change is termed *flow control*. In this intense area of research, methods are sought to delay laminar-to-turbulent transition, postpone flow separation, enhance lift, reduce drag, augment turbulence, or suppress noise. Our focus here is specifically velocity and concentration boundary layer control, where the boundary layer is manipulated to behave differently than it normally would along a smooth, straight surface. Specifically, we wish to impart an oscillatory component to the surface shear stress. Regardless of the mechanism of fouling, photographic evidence proves that growth occurs next to the membrane surface where the shear forces are low. We have suggested that tailored fluid/structure interactions can be a significant source of oscillation. Careful engineering is required to effect the desired conditions among these flow control methods; clearly, a perfect control strategy that is simple and does not have any trade-offs does not exist.

The influence of the mesh spacer on membrane shear stresses was evaluated using computation fluid dynamics (CFD) simulation of the Navier-Stokes equations. For geometries where portions of the mesh spacer are responding dynamically, the convenient dynamic mesh capability of the FLUENT™ code was used, with the motion of the dynamic element prescribed *a priori* from analytical formulae describing the natural frequency and forcing function. Only the initial unstructured tetrahedral mesh is required by the user of FLUENT; remeshing is done automatically. This computational approach is an effective screening tool prior to incurring the expense of coupled fluid-structure simulations and ultimately testing one-of-a-kind feed spacers.

Successful theoretical models of RO membranes consider both mass and momentum transfer phenomena to predict recovery. Al-Bastaki and Abbas (2000), for example, found good agreement with experimental recovery measurements when they defined the flux as an implicit function of the length and radius and integrated the function over the whole membrane.

An important phenomenon which encourages membrane fouling is *concentration polarization*. This effect, which is responsible for bringing too much salt to the membrane surface, can be understood through examination of the idealized flow between parallel plates.

With constant properties and steady-state conditions, the velocity and concentration profiles develop as shown in figure 1. The solute concentration increases from the bulk stream to a higher value at the membrane surface, while the velocity decreases from the bulk stream to the assumed no-slip condition at the wall. The velocity gradient at the wall determines the shear stress, which may result in foulant removal. If we introduce a feature to the feed spacer that responds dynamically, the local shear stress will be elevated locally and should reduce the tendency to foul and improve the permeate flux by interrupting the concentration boundary layer.

Several models have been used to predict membrane fouling (Barger and Carnahan, 1991):

- Gel polarization
  Momentum and concentration boundary layers develop adjacent to the membrane and are displaced by a layer of gel (polymerized species) that controls the flux.

- Resistance-in-series model
  Component resistances to the product flow, based on experiments and other submodels, are believed to act in series.

- Transport accumulation model
  Continuity, momentum, and species equations for soluble, slightly soluble, and organic solutes are solved iteratively.

While these models may be insufficient for general use, we expect that the models are sufficiently valid to establish trends.

3. Conclusions and Recommendations

- CFD simulations of a feed spacer from a spiral-wound RO cartridge indicate regions of low membrane shear stress in the middle of the spacer between the crossing filaments. Photographs of the membranes of an expired cartridge confirm the accumulation of foulants at these locations. Thus, elevating the shear stress at these locations would be beneficial.

- We examined vortex shedding from microcylinders between the membranes and fluttering ribbons in bending and torsion. The microcylinders were tried because of the potential to scrub the membranes with the junction vortices;[2] however, this method proved ineffective. The cantilevered, bending ribbons produced the largest changes in the flow field in view of the elevated salt concentration at the exit of the computational cell and the shear stress on the membranes.

- Our CFD analysis was quasi-steady because we prescribed the motion of the dynamic spacer element *a priori*, and there was no coupling between the fluid and the structure. From potential flow analyses of thin airfoils, response functions have been derived as a function of reduced frequency. We have extrapolated a reduced frequency from data taken for fluttering paper strips in air flow. The response functions indicate a reduction in response of 70 percent from the quasi-steady response. Even so, because the entire mesh spacer is comprised of several hundred thousand of these cells, the improvement is significant.

- The net cost in pressure drop of adding the dynamic element to the mesh spacer should be reduced because the phase relationship among the thousands of oscillating ribbons will not be inphase but random. We estimate that the increase in pressure drop will be approximately 10 percent.

- We recommend that a fully coupled simulation of the fluid/structure interaction be completed to include the real fluid effects and actual response of the structure to the time-dependent fluid loads. The simulation should focus on the cantilevered, bending ribbons.

- We recommend addressing the practicalities of mass manufacture of a feed spacer that would incorporate elements that are highly responsive to excitation from flow-induced forces.

[2] Junction vortices are formed when a protuberance from the boundary turns a component of the boundary layer vorticity in the streamwise direction. Common locations of junction vortices are the wing/fuselage intersection on aircraft, the conning tower/hull intersection on submarines, and bridge piers on a river bottom.

- The final design of the feed spacer could benefit from numerical design optimization. The design is constrained by a minimum channel height and support spacing necessary to keep the membrane leaves apart. Through a weighted objective function, we would seek to maximize the oscillating membrane shear stress and the exit concentration while minimizing the overall pressure drop through the channel.

4. Discussion

In this section, we introduce the components of a spiral-wound RO element and then describe the mesh spacer. Next, we present our computational approach to analyze the behavior of the spacer and our proposed modification with oscillating structural elements. We close with a brief discussion of flutter.

4.1 Spiral-wound Reverse Osmosis Elements

The spiral-wound (SW) element is the principal RO configuration in use today. Modules of SW elements benefit from high membrane density and low plant investment relative to other tubular, plate-and-frame, or hollow wide-fiber systems. These modules are easy to clean, but they have some tendency to foul. Principal types and variables of spiral-wound elements are given in table 1.

Table 1. Types and Variables of Spiral-Wound Elements (Wagner, 2001)

Dimensions	Outer diameter of element Length of element Internal diameter of the center tube
Outer wrap	Fiber glass; tape; several sanitary designs
End of element	Female connection; male connection
Center tube	Several types of polymers used
Brine spacer	0.75 millimeter (mm) (0.0295 inch [in]) 1.20 mm (0.0472 in) 2.30 mm (0.0906 in) Higher spaces are available
Spacer type	Diamond type (standard) Free channel
Membrane support	Polyester (standard) ; Polypropylene
Brine seal	U-cup seal; lip seal; no seal
Anti-telescoping device	Star-type; hole-plate type

The construction of an SW membrane element is shown in figure 2. An element may contain from one to a few dozen membrane leaves, depending on the diameter and element type. Each leaf is made of two membrane sheets glued together on three sides with support fabric in between; the open side is sealed against the perforated permeate core tube that collects the permeate from all leaves. The leaves are then rolled up with a mesh or net-type spacer between each of them to keep them apart. The membrane leaves have a large active area, while a thick feed spacer reduces fouling and increases the effectiveness of cleaning

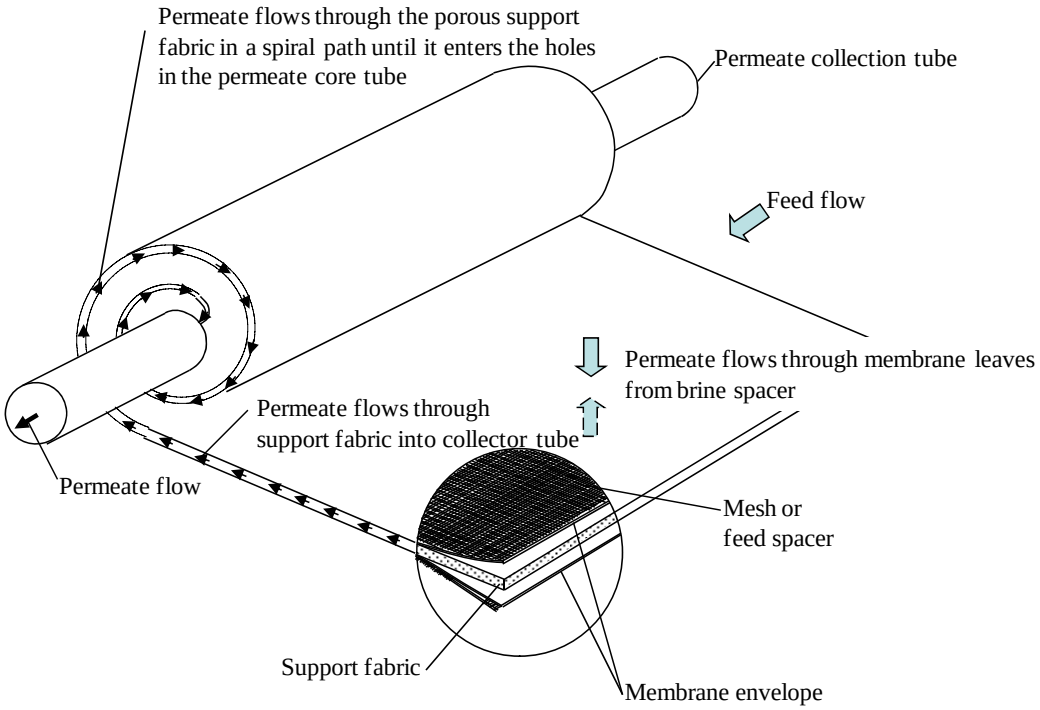

Figure 2. A single leaf of a spiral-wound reverse osmosis element.

operations (FILMTEC™ Reverse Osmosis Membranes, 2004). Kremen (1977) presents a concise treatment of the technological development of SW reverse osmosis membrane modules.

Our study focuses on the mesh spacer. Johnson (2005) noted that the ideal mesh spacer would:

- Have low resistance to feed flow
- Have a high density of contact points with the membrane so that nesting of the membrane envelopes is avoided
- Be very thin to maximize the amount of membrane area in an element of a given diameter
- Promote mixing to minimize concentration polarization
- Have a smooth surface to minimize the discriminating layer of the membrane
- Be inexpensive to manufacture and use

An optimal design balances these competing concerns.

The major problems for the membrane separation processes such as reverse osmosis are concentration polarization and fouling; both phenomena reduce the flux. Concentration polarization results from the strong convective transport of solutes to the membrane surface but the slower back-diffusion to the bulk. It is particularly prevalent for large solute molecules, high permeate fluxes, and low feed velocities in the axial direction. The adverse effects of concentration polarization are decreased permeation of water and increased passage of the salt into the permeate. Fouling is a deposition of foreign matter on the membrane surface which reduces the permeation rate. For a membrane application, reducing the concentration boundary layer can address both concentration polarization and fouling; however, remediation techniques are quite restricted inside the spiral-wound module. One effect of the mesh spacer is to promote turbulence locally, thereby reducing the polarization; unfortunately, the mixing comes at the expense of increased pressure drop.

Spiral-wound membrane modules are particularly susceptible to fouling where the mesh spacer contacts the membrane. During manufacturing, pressure is applied to the spacer as it is wrapped around the permeate core tube. The contact sites lower flow rates locally and increase the concentration of salts. Supersaturation at these sites may lead to nucleation and accumulation of foulants, provided a critical size is obtained. When the precipitated salt adheres to the wetted surface, scale formation occurs, encouraging the proliferation of nucleation sites for subsequent crystal growth. Pervov (1991) provided photographic evidence that the fouling originates at the sites where the membrane and spacer contact, and our photograph of a fouled membrane leaf in figure 3 confirms this conclusion. Reduction of the adhesion tendency can lessen or eliminate the production of scale. In multistage flash plants, scales of calcium sulfate, magnesium hydroxide, and calcium carbonate are persistent; but in RO plants, the adhesion of biofouling to the membrane is often the problem (Al-Ahmad and Aleem, 1994). If these adhesion forces can be successfully countered by modification of the mesh spacer design, the problem and cost of scaling and fouling can be reduced. Current treatment methods involve chemicals and flushing procedures; the effort described herein focuses on the geometric tailoring of the mesh spacer so that fouling can be reduced during normal operation.

The benefit of reduced fouling from the mesh spacer design is applicable wherever spiral-wound membrane elements are used. The technical risk rests in the ability to:

- Achieve elevated shear stresses at the membrane without significantly increasing the overall pressure drop of the feed flow and reducing the permeate flux

- Generate a sufficient vibratory response without structural failure

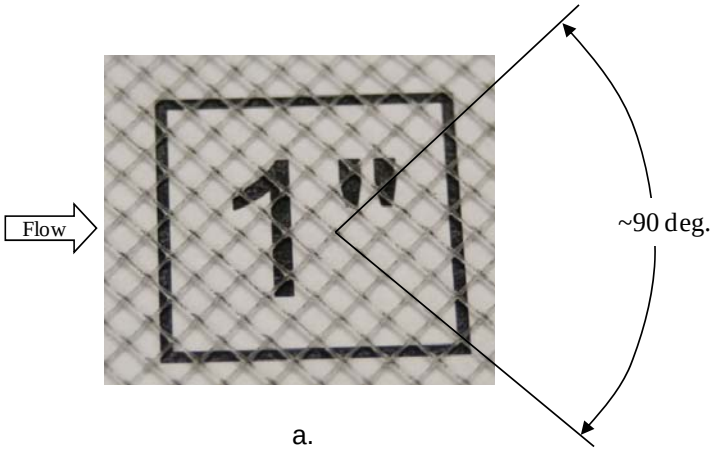

a.

b.

1 inch = 25.4 mm

Figure 3. An isolated feed spacer (a.) and one of the adjoining fouled membranes (b.).

4.2 Mesh Spacer

Prior to starting the CFD modeling, we purchased two expired seawater reverse osmosis (SWRO) elements from a local drinking water provider. We split one of the cartridge casings in order to examine the actual geometry and fouling behavior of the SWRO element as shown in figure 4. The SWRO element was a FilmTec™ Model XLE-4040 with the performance characteristics provided in table 2.

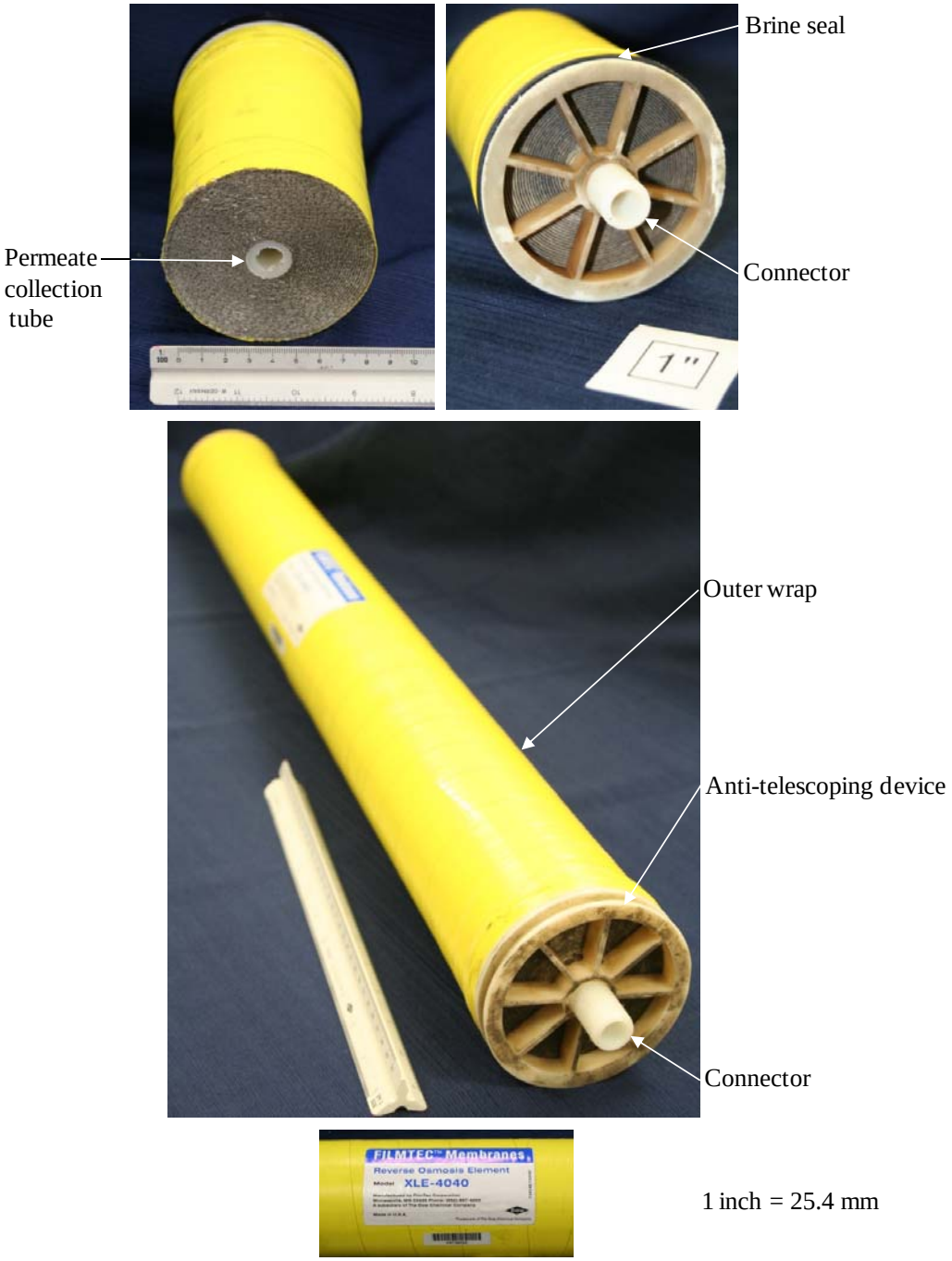

Figure 4. FilmTec™ XLE-4040 extremely low energy reverse osmosis element of 102-mm (4-in) nominal diameter and 1.02-m (40-in) overall nominal length.

Table 2. Performance Characteristics of the FilmTec™ XLE-440 Membrane Element[1]

Membrane Type	Polyamide Thin-Film Composite
Maximum operating temperature	45 °C (113° F)
Maximum operating pressure	4.137MPa (600 psi)
Maximum pressure drop	89.6 kPag (13 psig)
Standard Test Conditions	
Feedwater	NaCl, 500 ppm
Temperature	25 °C (77 °F)
Pressure	0.689 MPa (100 psi)
pH	8
Recovery	15%
Product Specifications (Part No. 154530)	
Active area	8.08 m^2 (87 ft^2)
Applied pressure	0.689 MPa (100 psi)
Permeate flow rate	0.114 L/s (2,600 gal/day)
Stabilized salt rejection	99.0 %
Maximum feed flow rate	0.883 L/s (14 gal/min)

[1] ppm = parts per million; °C = degrees Celsius; °F = degrees Fahrenheit; MPa = megapascal; % = percent; m^2 = square meters; ft^2 = square foot; psi= pounds per square inch; kPag = kilopascal gauge; psig = pound per square inch gauge; NaCl = sodium chloride; L/s = liter per second; gal/day = gallons per day; gal/min = gallons per minute.

While the main function of spacers is to keep the membrane leaves apart, they are also designed to increase mass transfer by promoting mixing while minimizing the requisite pressure loss. Moreover, the spacers help distribute the flow more evenly among the many parallel channels in the SWRO element. Their effectiveness varies as a function of the filament diameter, mesh length, channel height, the angle between the filaments, and the angle of the filaments with respect to the main flow direction. Among these, the primary characteristics are the channel height and the channel void fraction.

A key aspect of contemporary mesh spacer designs is *strand thinning*—a narrowing of the filaments between crossing points. With this feature, the volume of the strands and, hence, the pressure drop are reduced while maintaining the channel height. Flux enhancements of three to five times have been reported for spacer-filled channels compared to empty channels, but fouling cannot be avoided in some feeds (Schwinge, Wiley, and Fane, 2004). A dimensionless spacer-flux-to-pressure-loss-ratio was defined as a measure of goodness to compare the spacer

designs. The zigzag arrangement—when the transverse filaments are located alternately between the top and bottom wall—showed the highest permeate flux and the lowest pressure loss for low flow rates from two-dimensional simulations by Schwinge, Wiley, and Fletcher (2002b, 2002c). The filaments of XLE-4040 have both the strand thinning and the zigzag arrangement. Moreover, the hydrodynamic angle—the 90-degree angle in figure 3—is optimum for increased permeate flux as recorded by Da Costa and Fane (1994).

The mesh spacer has a Reynolds number definition, Re_{Dh}, given by

$$\mathrm{Re}_{Dh} = \frac{d_h u_{ave}}{\nu} \tag{1}$$

where d_h is the hydraulic diameter:

$$d_h = \frac{4\varepsilon}{\frac{2}{h_{ch}} + (1-\varepsilon) S_{vsp}} = \frac{4(V_{tot} - V_{sp})}{S_{slit} + S_{sp}} \tag{2}$$

A Reynolds number can also be defined based on the channel height:

$$\mathrm{Re}_{ch} = \frac{h_{ch} u_{ave}}{\nu} \tag{3}$$

For the Model XLE-4040 mesh spacer, the two Reynolds number definitions are related by

$$\mathrm{Re}_{Dh} = 1.44\,\mathrm{Re}_{ch} \tag{4}$$

The specific surface area of the spacer is

$$S_{vsp} = \frac{S_{sp}}{V_{sp}} \tag{5}$$

The ratio of the volume of empty space in the channel to the volume of the channel is given by

$$\varepsilon = \frac{V_{tot} - V_{sp}}{V_{tot}} \tag{6}$$

Parameters relevant to hydraulic diameter calculation for the XLE-4040 element are presented in table 3.

Table 3. Flow Parameters for XLE-4040[1]

Channel height, h_{ch}	0.724 mm (0.0285 in)
Hydraulic diameter, d_h	1.04 mm (0.041 in)
Specific surface area of the spacer, S_{sp}	12.4 per mm (314.0 per in)
Volume of the channel, V_{tot}	14.8 mm^3 (0.000905 in^3)
Volume of the spacer, V_{sp}	0.983 mm^3(0.000060 in^3)
Surface area of the empty channel (slit), S_{slit}	41.0 mm^2 (0.06350 in^2)
Surface area of the spacer, S_{sp}	12.2 mm^2 (0.01884 in^2)
Voidage of the spacer filled channel, ε	93.37 percent
Channel Reynolds number, Re_{ch}	284
Average velocity in the channel, u_{ave}, for standard test conditions	0.239 m per second (9.4 in per second)
Dynamic viscosity, μ	0.890 cP
Density, ρ	996 kg per m^3 (62.2 lb per ft^3)
Kinematic viscosity, ν	8.932(10^{-7}) m^2 per second (9.614(10^{-6}) ft^2 per second)

[1] mm^3= cubic millimeter; mm^2 = square millimeter; in^3= cubic inch; in^2= square inch; kg = kilogram; m^3= cubic meter; m^2= square meter; lb = pound; ft^3= cubic foot.

The pressure loss along the channel can be used to determine a Fanning friction factor which varies as a function of the Reynolds number

$$f = \frac{\tau}{\frac{1}{2}\rho u^2} = \frac{\Delta p_{ch} d_h}{\rho u^2 L} = \frac{A'}{Re} + \frac{B'}{Re^n} \tag{7}$$

The value of the exponent *n* is an indication of the flow regime:

$n < 0.25$ highly turbulent (8)

$n = 1$ laminar (9)

$0.25 \leq n < 1$ transition (10)

The flow characteristics of microcylinders with their axis along the channel wall vary as the Reynolds number is increased:

- Re > 200: periodic motions begin as flow becomes unsteady
- Re > 600: a large eddy is formed behind the cylinder; flow is fully unsteady

Eddies downstream and upstream of the filament enhance mass transfer. As the filaments move closer together, the distance between the peaks in the shear stress is reduced, thereby increasing mass transfer. Eddy sizes vary with Reynolds number.

Two-dimensional simulations (Schwinge, Wiley, and Fletcher, 2002a) show complex relationships between the flow patterns, pressure loss, shear stress on the walls, filament configuration, mesh lengths, filament diameters, and Reynolds number in narrow and obstructed channels. Recirculation regions are formed before and after each filament, with the size and shape of the regions being dependent on the spacer configuration, filament diameter, mesh length, and Reynolds number. An effective spacer provides a high mass-transfer rate from the membrane wall toward the bulk stream to reduce the wall concentration while a low-pressure loss is maintained along the channel.

4.3 Computational Approach

The CFD analysis was completed using FLUENT™ version 6.2.16, a finite volume Navier-Stokes solver. The fluid region was discretized into a finite set of control volumes, using FLUENT's mesh generator GAMBIT™. Conservation equations were solved for mass, momentum, and species, etc. For the current three-dimensional problem, five conservation equations apply for the incompressible, isothermal, laminar flow of the brackish feed through the mesh spacer.

- Mass conservation or continuity

$$\frac{1}{\rho}\frac{\partial \rho}{\partial t}+\frac{\partial u}{\partial x}+\frac{\partial v}{\partial y}+\frac{\partial w}{\partial z}=0 \tag{11}$$

- *x*-momentum

$$\frac{\partial u}{\partial t}+u\frac{\partial u}{\partial x}+v\frac{\partial u}{\partial y}+w\frac{\partial u}{\partial z}=\frac{1}{\rho}\left[-\frac{\partial p}{\partial x}+\frac{\partial \tau_{xx}}{\partial x}+\frac{\partial \tau_{xy}}{\partial y}+\frac{\partial \tau_{xz}}{\partial z}\right]+F_x \tag{12}$$

- *y*-momentum

$$\frac{\partial v}{\partial t}+u\frac{\partial v}{\partial x}+v\frac{\partial v}{\partial y}+w\frac{\partial v}{\partial z}=\frac{1}{\rho}\left[-\frac{\partial p}{\partial y}+\frac{\partial \tau_{yx}}{\partial x}+\frac{\partial \tau_{yy}}{\partial y}+\frac{\partial \tau_{yz}}{\partial z}\right]+F_y \tag{13}$$

- *z*-momentum

$$\frac{\partial w}{\partial t}+u\frac{\partial w}{\partial x}+v\frac{\partial w}{\partial y}+w\frac{\partial w}{\partial z}=\frac{1}{\rho}\left[-\frac{\partial p}{\partial z}+\frac{\partial \tau_{zx}}{\partial x}+\frac{\partial \tau_{zy}}{\partial y}+\frac{\partial \tau_{zz}}{\partial z}\right]+F_z \tag{14}$$

- Species transport

$$\frac{\partial c}{\partial t}+u\frac{\partial c}{\partial x}+v\frac{\partial c}{\partial y}+w\frac{\partial c}{\partial z}=D\left(\frac{\partial^2 c}{\partial x^2}+\frac{\partial^2 c}{\partial y^2}+\frac{\partial^2 c}{\partial z^2}\right) \tag{15}$$

For turbulent flow, we have

- Mass conservation or continuity

$$\frac{1}{\rho}\frac{\partial \rho}{\partial t}+\frac{\partial u}{\partial x}+\frac{\partial v}{\partial y}+\frac{\partial w}{\partial z}=0 \tag{16}$$

- *x*-momentum

$$\frac{\partial u}{\partial t}+u\frac{\partial u}{\partial x}+v\frac{\partial u}{\partial y}+w\frac{\partial u}{\partial z}=\frac{1}{\rho}\left[-\frac{\partial p}{\partial x}+\frac{\partial\left(\tau_{xx}-\rho\overline{u'u'}\right)}{\partial x}+\frac{\partial\left(\tau_{xy}-\rho\overline{u'v'}\right)}{\partial y}+\frac{\partial\left(\tau_{xz}-\rho\overline{u'w'}\right)}{\partial z}\right]+F_x \tag{17}$$

- *y*-momentum

$$\frac{\partial v}{\partial t}+u\frac{\partial v}{\partial x}+v\frac{\partial v}{\partial y}+w\frac{\partial v}{\partial z}=\frac{1}{\rho}\left[-\frac{\partial p}{\partial y}+\frac{\partial\left(\tau_{yx}-\rho\overline{v'u'}\right)}{\partial x}+\frac{\partial\left(\tau_{yy}-\rho\overline{v'v'}\right)}{\partial y}+\frac{\partial\left(\tau_{yz}-\rho\overline{v'w'}\right)}{\partial z}\right]+F_y \tag{18}$$

- *z*-momentum

$$\frac{\partial w}{\partial t}+u\frac{\partial w}{\partial x}+v\frac{\partial w}{\partial y}+w\frac{\partial w}{\partial z}=\frac{1}{\rho}\left[-\frac{\partial p}{\partial z}+\frac{\partial\left(\tau_{zx}-\rho\overline{w'u'}\right)}{\partial x}+\frac{\partial\left(\tau_{zy}-\rho\overline{w'v'}\right)}{\partial y}+\frac{\partial\left(\tau_{zz}-\rho\overline{w'w'}\right)}{\partial z}\right]+F_z \tag{19}$$

- Species transport

$$\frac{\partial c}{\partial t}+u\frac{\partial c}{\partial x}+v\frac{\partial c}{\partial y}+w\frac{\partial c}{\partial z}=D\left[\frac{\partial^2 c}{\partial x^2}+\frac{\partial^2 c}{\partial y^2}+\frac{\partial^2 c}{\partial z^2}\right]-\frac{\partial}{\partial x}\overline{u'c'}-\frac{\partial}{\partial y}\overline{v'c'}-\frac{\partial}{\partial z}\overline{w'c'} \tag{20}$$

In order to solve the set of governing equations for turbulent flow, i.e., the Reynolds-averaged Navier-Stokes (RANS) equations, it is necessary to make assumptions about the turbulence correlations denoted by the primed variables and the overbar. These assumptions form the basis of the turbulence model, which must be verified by comparison with experimental measurements. Boussinesq (ctd. in Tannehill et al., 1997) related the turbulent shearing stresses to the rate of mean strain through an apparent eddy viscosity, ν_t. Most turbulence models used to solve the RANS equations are based on a relation of this type. Turbulence models are further classified by the number (zero to twelve) of partial differential equations that must be solved to supply the modeling parameters. In this study, we used the two-equation κ - ε_t turbulence model based on renormalization group (RNG) theory and the one-equation Spalart-Allmaras model (ctd. in Tannehill et al., 1997), where

$$\kappa = \frac{1}{2}\left(\overline{u'u'} + \overline{v'v'} + \overline{w'w'}\right) \tag{21}$$

and the turbulent eddy viscosity is

$$\nu_t = C_\mu \frac{\kappa^2}{\varepsilon_t} \tag{22}$$

The RNG κ - ε_t turbulence model accounts for low-Reynolds-number effects much better than the standard κ - ε_t model; in the channel flow of RO, the low Reynolds number, anisotropic eddy activities are very important (Cao et al., 2001). In the Spalart-Allmaras model, the transported variable is a variation of the turbulent eddy viscosity rather than the turbulence kinetic energy or turbulence dissipation rate. It also has the advantage of the lowest computational burden among all of the turbulence models available in FLUENT. For turbulent diffusion, a default value of 0.7 was used for the turbulent Schmidt number,

$$\mathrm{Sc}_t = \frac{\nu_t}{D_t} \tag{23}$$

FLUENT employs a solution algorithm in which the governing equations are solved sequentially. Because the governing equations are non-linear and coupled, an iterative procedure must be used, as outlined below.

1. The *x*-, *y*-, and *z*-momentum equations are each solved in turn.

2. A pressure correction equation is solved to obtain the necessary corrections to the pressure and velocity fields so that continuity, or conservation of mass, is satisfied.

3. The scalar equation(s)—species transport, turbulence kinetic energy, turbulence dissipation rate, or modified turbulent eddy viscosity—are solved using the updated values of the other variables.

4. A check for convergence of the equations is made by examining the residual (i.e., the degree of unbalance, for each governing equation).

While there are no universal metrics for judging convergence, we accept the solution as meaningful when the scaled residuals have decreased at least three orders of magnitude and remain nearly unchanged with further iteration. The rate of convergence is controlled by the magnitude of the under-relaxation factors and the discretization methods. Program default values were used generally.

Our computations used both two-dimensional and three-dimensional computational domains. The three-dimensional computational domain is one repeating section of the mesh spacer as shown in figure 5. This domain is bounded by the inlet and exit planes, two periodic planes, and the walls formed by the membrane above and below the mesh spacer.

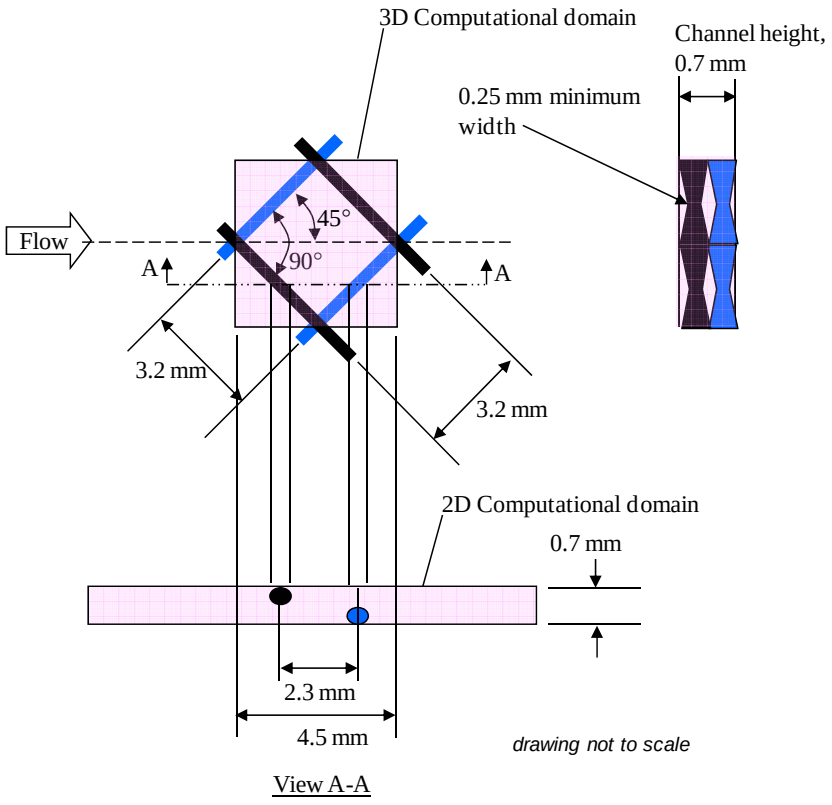

Figure 5. Two- and three-dimensional computational domains from a repeating section of the mesh spacer from the XLE-4040 reverse osmosis element.

A number of boundary conditions were imposed depending on the simulation objective and the dimensionality of the computational domain. These are illustrated in figure 6 for the two-dimensional domain and in figure 7 for the three-dimensional domain.

- For both the two- and three-dimensional empty-channel domains, the inlet and exit planes were made translational periodic (i.e., the corresponding inlet and exit planes have the same velocity field by definition). Thus, we are able to compute a fully developed velocity profile and associated pressure gradient. This velocity profile can be used as an inlet profile for subsequent calculations with the mesh spacer present.

- The no-slip condition was applied at the surface of the filaments and the channel and membrane surfaces above and below the mesh spacer. Where salt transport was simulated, the membrane surfaces were assigned a high concentration value to simulate polarization.

- Periodicity was established along the planes perpendicular to the inlet and outlet and the membranes (i.e., the velocity and pressure fields are identical in these planes).

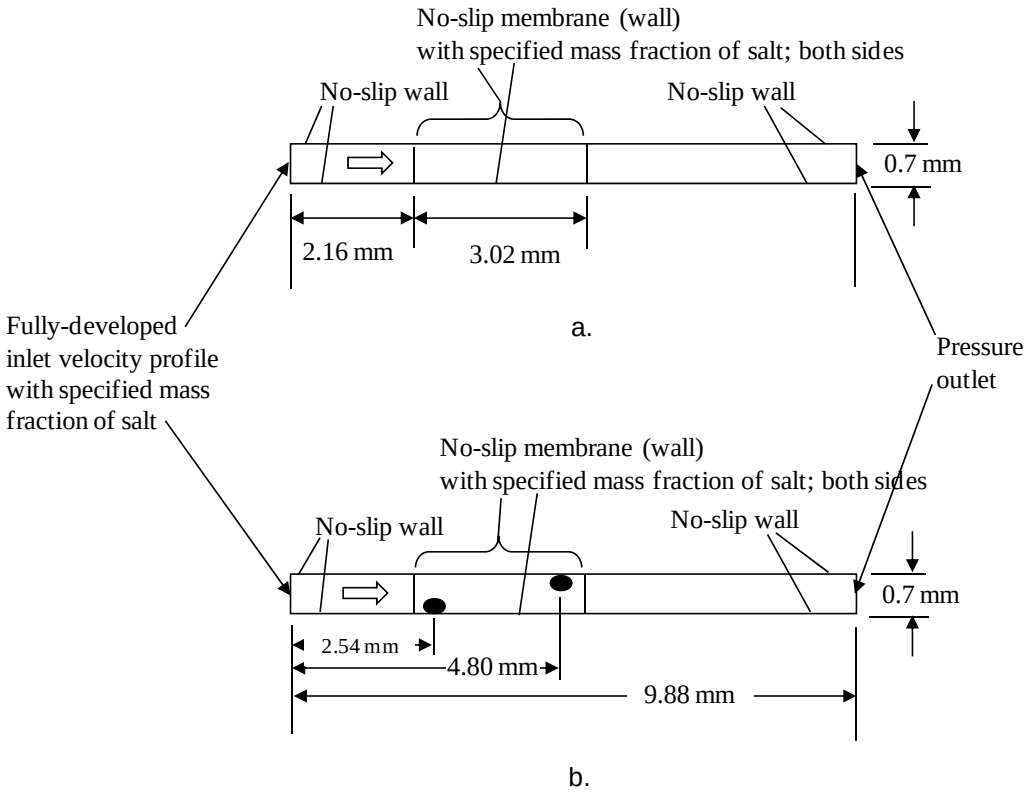

Figure 6. Two-dimensional computational domains for (a.) the plain (empty) channel or slit and (b.) channel with the two filaments in a zigzag arrangement.

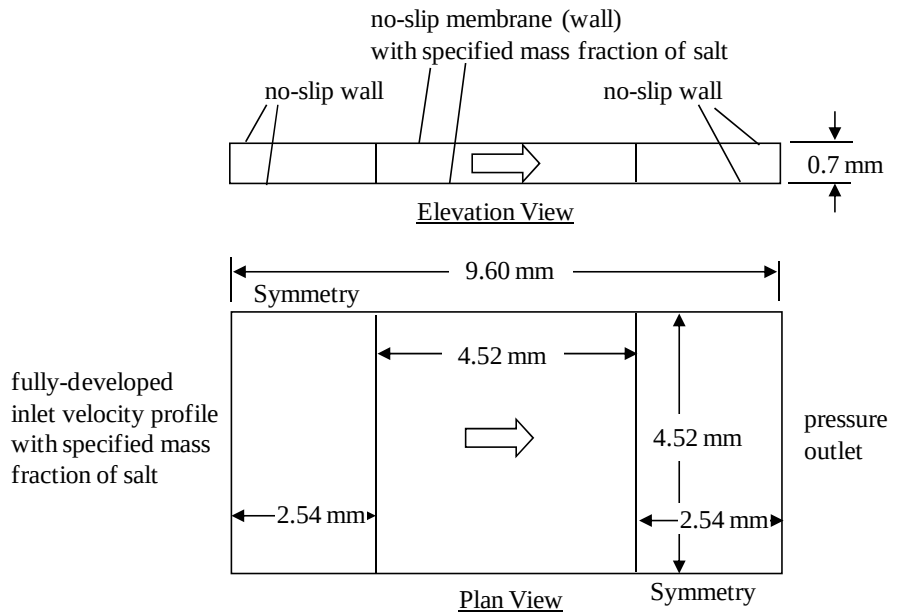

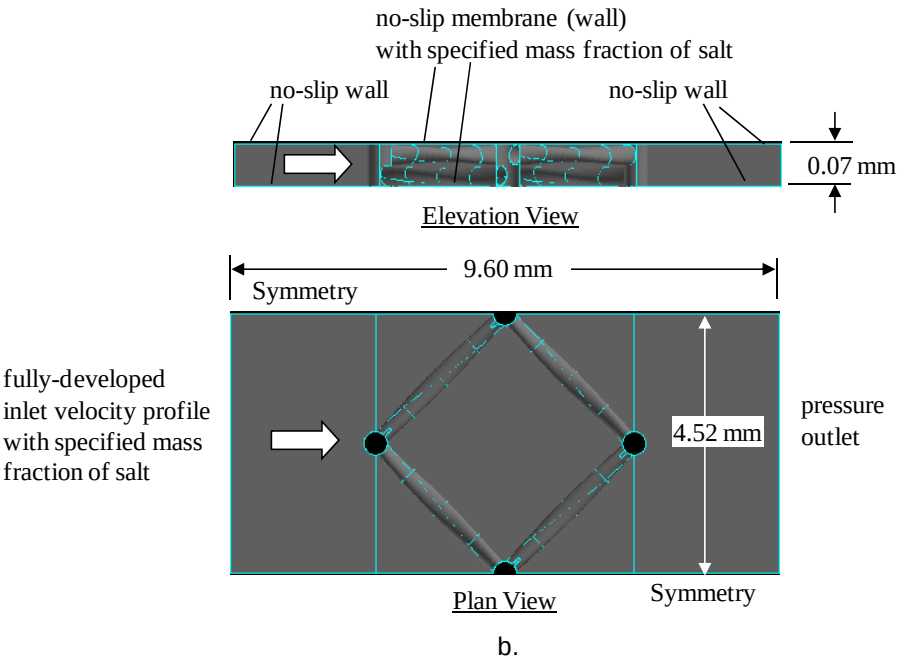

Figure 7. Three-dimensional computational domains for (a.) the plain channel and (b.) channel with the mesh spacer.

For some simulations with dynamic structural elements, the computational domain was changing shape as a function of time; and the dynamic mesh model in FLUENT was used. As the domain deformed as prescribed in a user-defined function, the volume mesh was updated automatically by FLUENT at each time step.

We considered two dynamic elements: a fluttering cantilevered beam or ribbon and a ribbon in torsional oscillation.

We used the fundamental mode for a cantilevered beam:

$$\Phi_1\left(\frac{x}{c_\ell}\right)=\cosh\left(\lambda_1\frac{x}{c_\ell}\right)-\cos\left(\lambda_1\frac{x}{c_\ell}\right)-\sigma_1\left(\sinh\left(\lambda_1\frac{x}{c_\ell}\right)-\sin\left(\lambda_1\frac{x}{c_\ell}\right)\right) \tag{24}$$

so that the normalized displacement is defined by

$$\eta_1\left(\frac{x}{c_\ell},t\right)=\Phi_1\left(\frac{x}{c_\ell}\right)\sin(\omega_1 t) \tag{25}$$

For the first mode,

$$\lambda_1=1.875 \tag{26}$$

$$\sigma_1=0.734 \tag{27}$$

$$\omega_1=\frac{\lambda_1^2}{c_\ell^2}\left(\frac{EI}{W_e}\right)^{\frac{1}{2}} \tag{28}$$

For the torsional oscillation, the normalized twist angle is given by

$$\Theta\left(\frac{x}{c_\ell},t\right)=\left[\cos\left(2\pi\frac{x}{c_\ell}\right)-1\right]\sin(\omega_1 t) \tag{29}$$

Accordingly, the maximum rotation of the element occurs in the center, with zero rotation at the ends. Because we are solving the equations of fluid motion only with a quasi-steady assumption, we have prescribed amplitudes *a priori* based on the geometry of the XLE-4040 element in figure 5. The optimized configuration of the dynamic element would likely involve geometric changes to the mesh spacer to maximize the intended response.

In addition to the oscillating structures within the feed spacer, we also considered that the junction vortices formed around the base of a bluff structure spanning the channel may be beneficial in scrubbing the membrane locally. The erosive power

of these flow features can be compared to those around the base of old bridge support structures in rivers. In modern designs, the supports are faired into the riverbed to mitigate the erosion. For the feed spacer, the features are too small and the Reynolds number too low to generate a significant shear stress.

4.4 Simulation Results

We first simulated steady laminar flow of water at standard conditions in an empty channel of 0.7-mm height to compare our results with laminar theory. Using the translational periodic boundary condition, we predicted the pressure gradient and, hence, the friction coefficient for fully developed flow. Our results are nearly coincident with laminar theory as shown in figure 8, which predicts that

$$f = \frac{12}{Re_{ch}} = \frac{\Delta p_{ch}\, h_{ch}}{L} \frac{1}{\rho V^2} \tag{30}$$

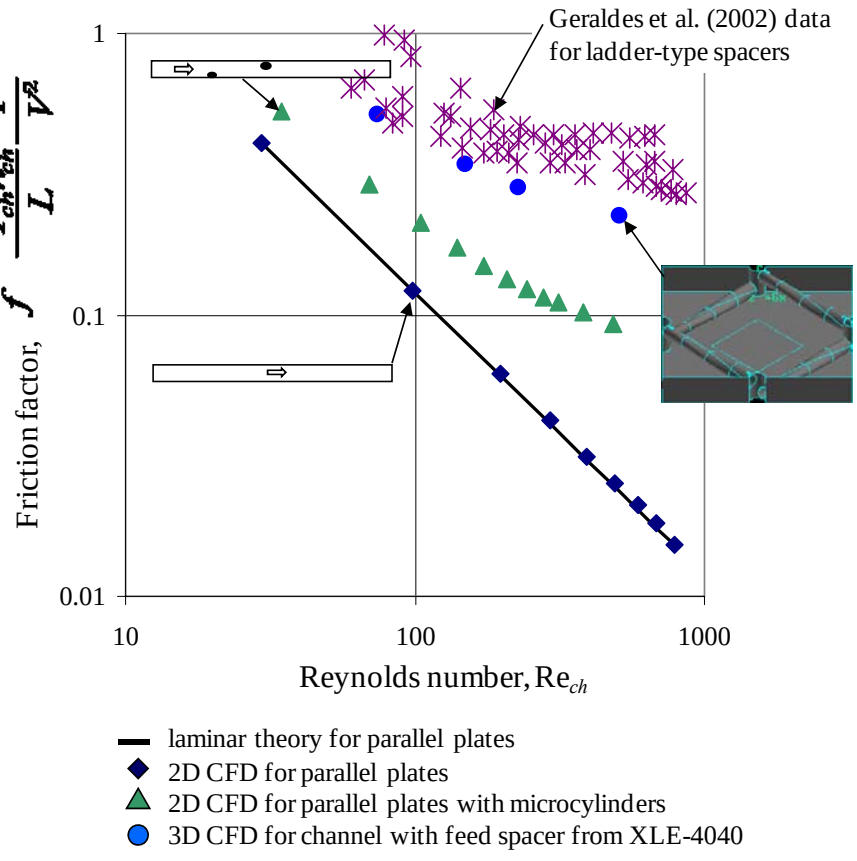

Figure 8. Friction factor versus channel Reynolds number for the feed channel.

The introduction of the pair of zigzag elements elevates the friction factor as we expect because of the pressure and skin friction drag of the elements themselves, but also as a result of the enhanced mixing in the wakes. At a Reynolds number, Re_{ch}, of around 400, we begin to see the flow downstream of the aft cylinder become unsteady as shown in figure 9. At $\mathrm{Re}_{ch} = 550$, the unsteadiness is more clear; and at $\mathrm{Re}_{ch} = 2{,}000$, it is obvious. Recall that the critical Reynolds number for transition to turbulence in pipe flow is 2,300.

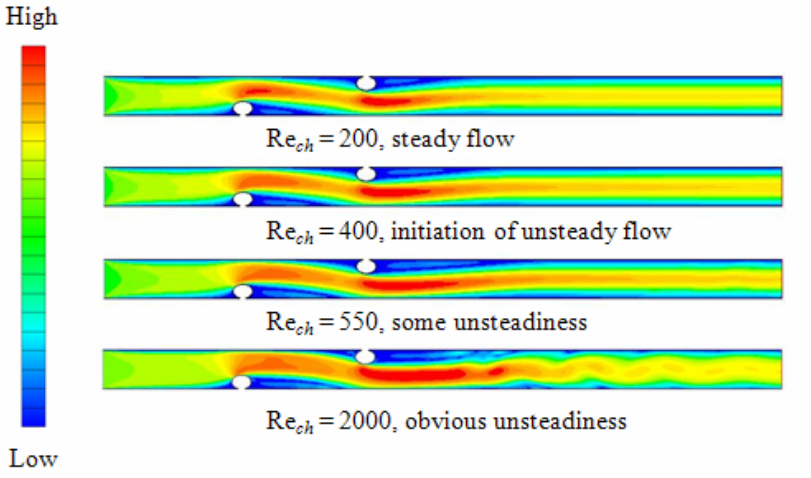

Figure 9. Velocity contours from two-dimensional simulations as a function of Reynolds number.

There is a significant amount of ambiguity in the literature regarding the actual onset of turbulent flow and the onset of laminar, periodic motions. Turbulent flow is characterized by random, nondeterministic motions; while the laminar, periodic motions are deterministic. Both promote mixing. While vortex streets behind cylinders in the free-stream are well known, the behavior in spacer-filled channels is relatively unknown. Clearly, the location and magnitude of the high shear stress regions and the eddies are related to the filament size and position. Investigators have used both laminar and turbulent simulations of the mesh spacer. For our baseline inlet velocity of 0.2 meters per second ($\mathrm{Re}_{ch} = 150$ or $\mathrm{Re}_{Dh} = 215$), we simulated both regimes.

Results from laminar three-dimensional simulations of the flow in a single repeating element of the mesh spacer are also plotted in figure 8. The friction factors are near the lower boundary of experimental data reported by Geraldes et al. (2002) for ladder-type spacers. The simulation at the highest Reynolds number showed some unsteadiness that made convergence more difficult. These three-dimensional simulations had 1.5 million tetrahedrons; our

subsequent grid independence study showed that we could reduce the cell count by up to 80 percent and capture the pressure drop within 2 percent.

Velocity contours on a three-dimensional periodic model of the XLE-4040 mesh spacer are illustrated in figure 10 for nine equally spaced planar cuts through the flow domain. Regions of local acceleration are apparent as the flow contracts through the restricted passages formed by the intertwined filaments. The downstream side of each filament contains a wake region of low velocity. The asymmetry of the velocity profile entering the cell can be viewed in figure 11(a). The region of maximum velocity is displaced towards the one of the membrane walls. The streamlines contract to pass through the constriction formed by the next downstream filament. The result is high levels of shear stress (figure 11(b)) resulting from the high strain rate (figure 11(c)).

Figure 12 illustrates the effect of the enhancement in mass transfer for the mesh spacer elements. For these simulations, the inflow has a salt concentration of 0.1; and the membrane surfaces have a salt concentration of 0.8 to simulate concentration polarization. A metric of goodness is, therefore, the ratio of the outlet concentration to the inlet concentration, $\frac{c_{out}}{c_{in}}$. The two-dimensional simulations indicate a 2- to 4-percent improvement in mass transfer from a comparison of the laminar simulations with and without the zigzag elements. The mesh spacer shows a 2- to 16-percent improvement in mass transfer over a plain three-dimensional channel.

Based in part on our modeling of the XLE-4040 mesh spacer configuration, we proceeded to analyze the effect of a dynamically responding structural element as shown in figure 13. Figure 13(a) shows a thin cantilevered ribbon that moves or flutters in response to flow along it. Figure 13(b) shows a ribbon spanning two support beams that twists about its axis. Even before numerical analysis, we expect that the cantilevered ribbon would have a greater area of influence and, thus, greater potential to interrupt the concentration boundary layer.

Because the computational domain is deforming as a function of time, FLUENT's dynamic mesh capability was used to re-mesh the domain at each time step as shown in figure 14 for a fixed-free beam oscillating in a two-dimensional channel. We then transferred the user-defined function prescribing this motion to the cantilevered ribbon embedded within the XLE-4040 mesh as shown in figure 13(a).

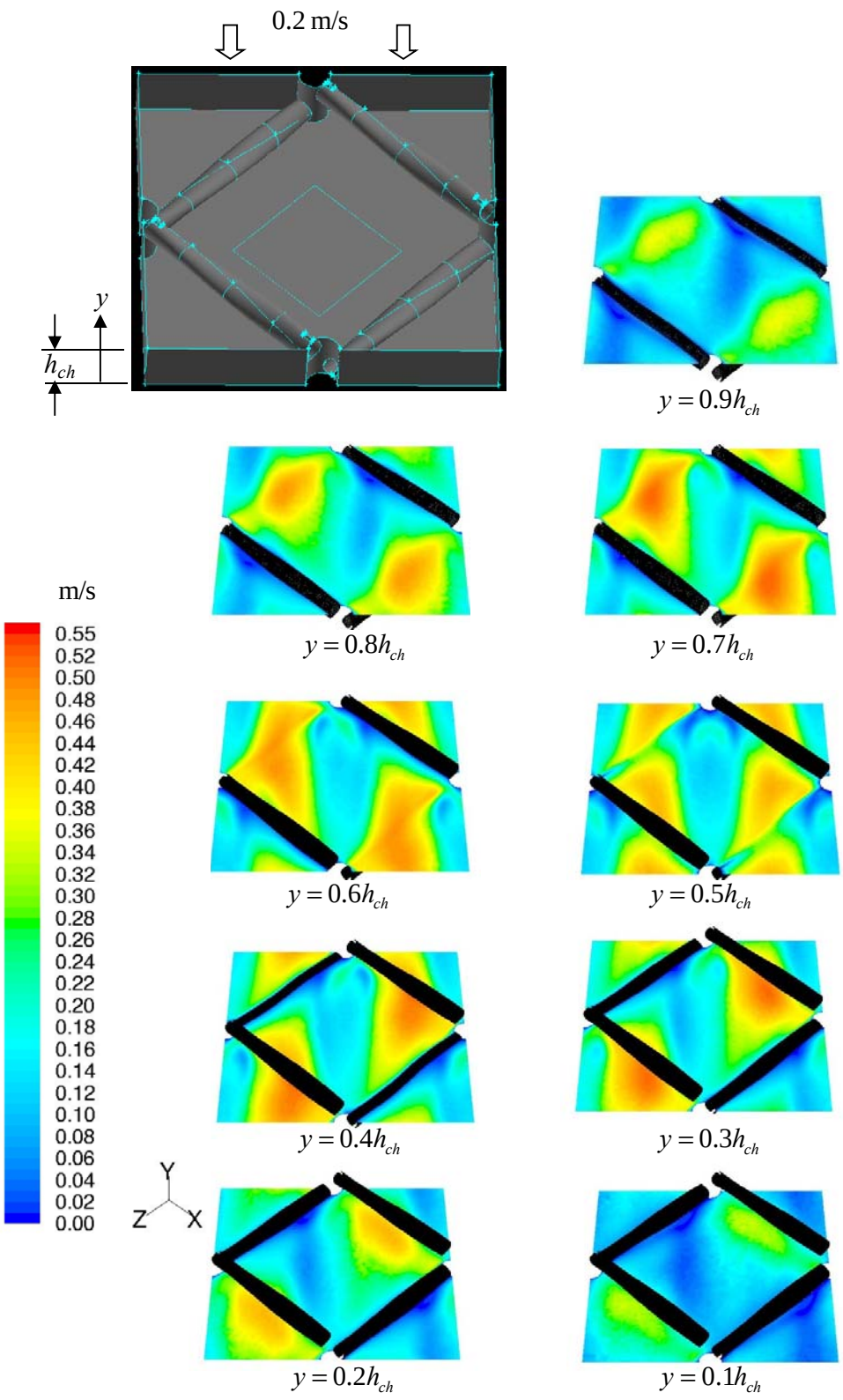

Figure 10. Contours of velocity magnitude in planes of constant *y*.

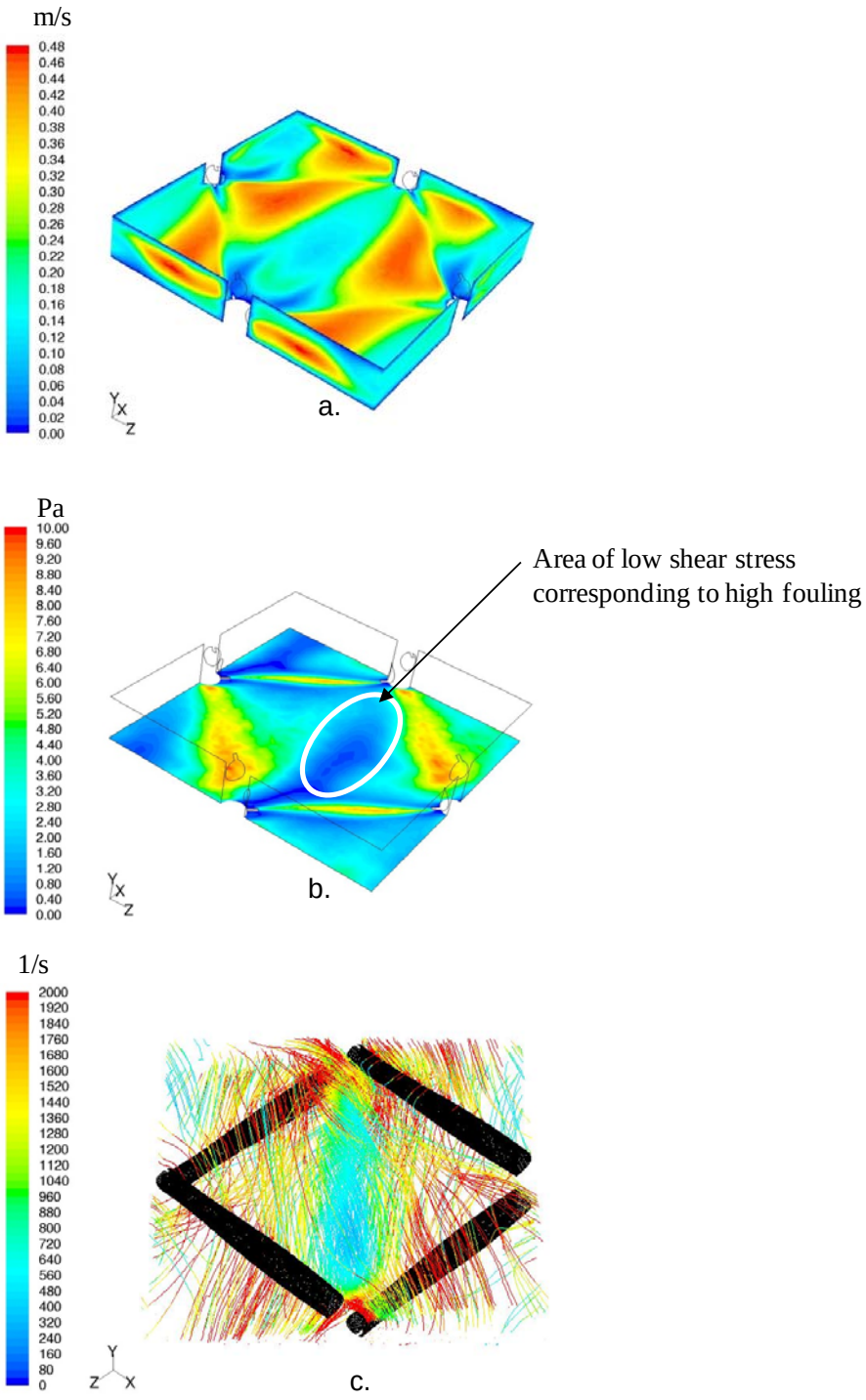

Figure 11. CFD simulation results for baseline membrane: (a.) velocity magnitude on midplane and periodic boundaries, (b.) shear stress contours on bottom wall, and (c.) path lines colored by strain rate.

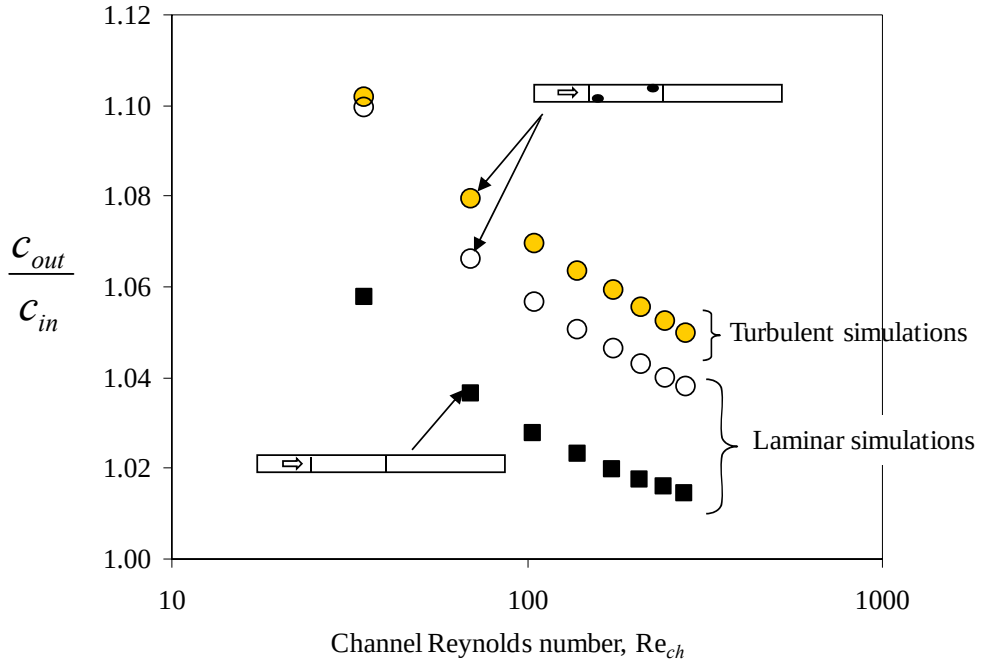

a.

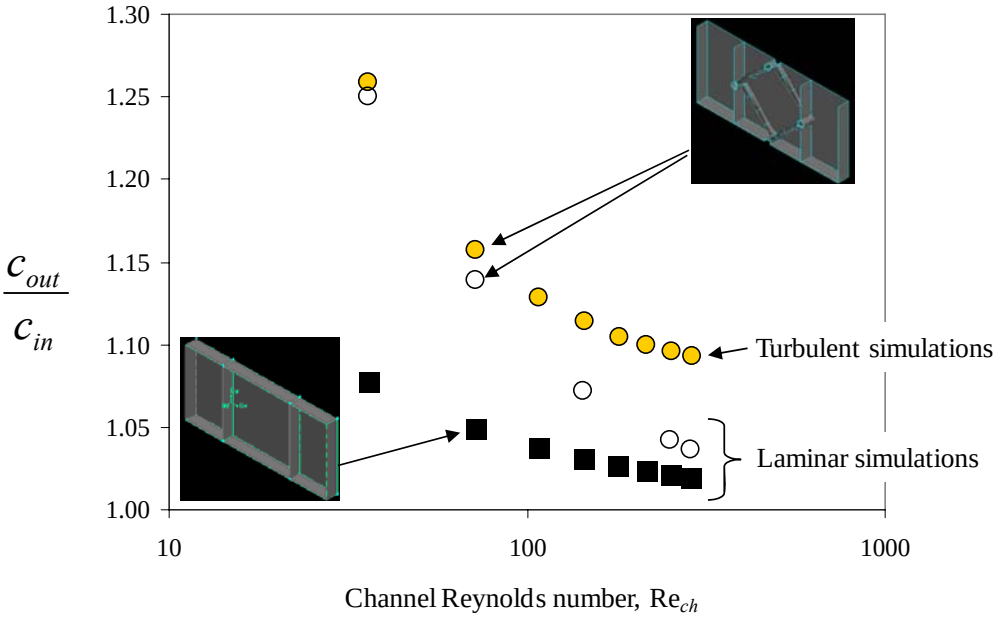

b.

Figure 12. Computed mass transfer enhancement for (a.) two-dimensional simulation and (b.) three-dimensional simulation.

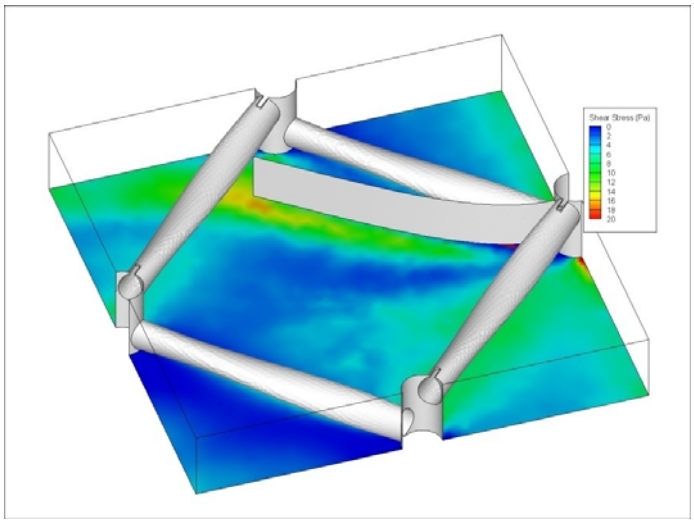

a.

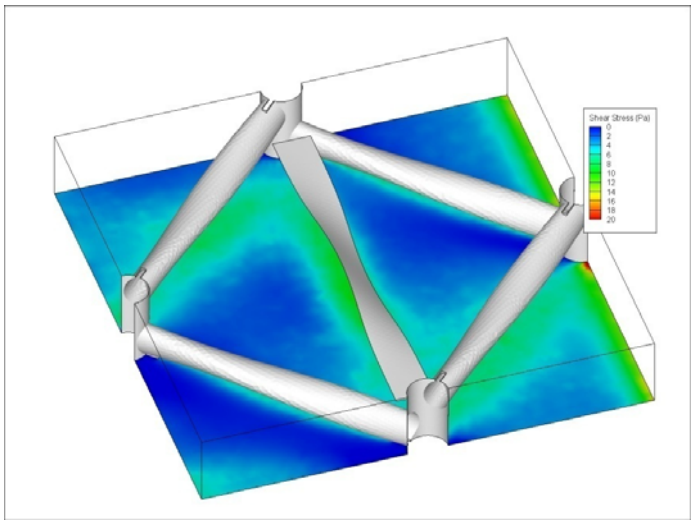

b.

Figure 13. Designs of dynamic structural elements in a feed spacer: (a.) bending element of 0.51-mm width by 2.54-mm length and (b.) torsional element 0.51 mm by 4.12 mm.

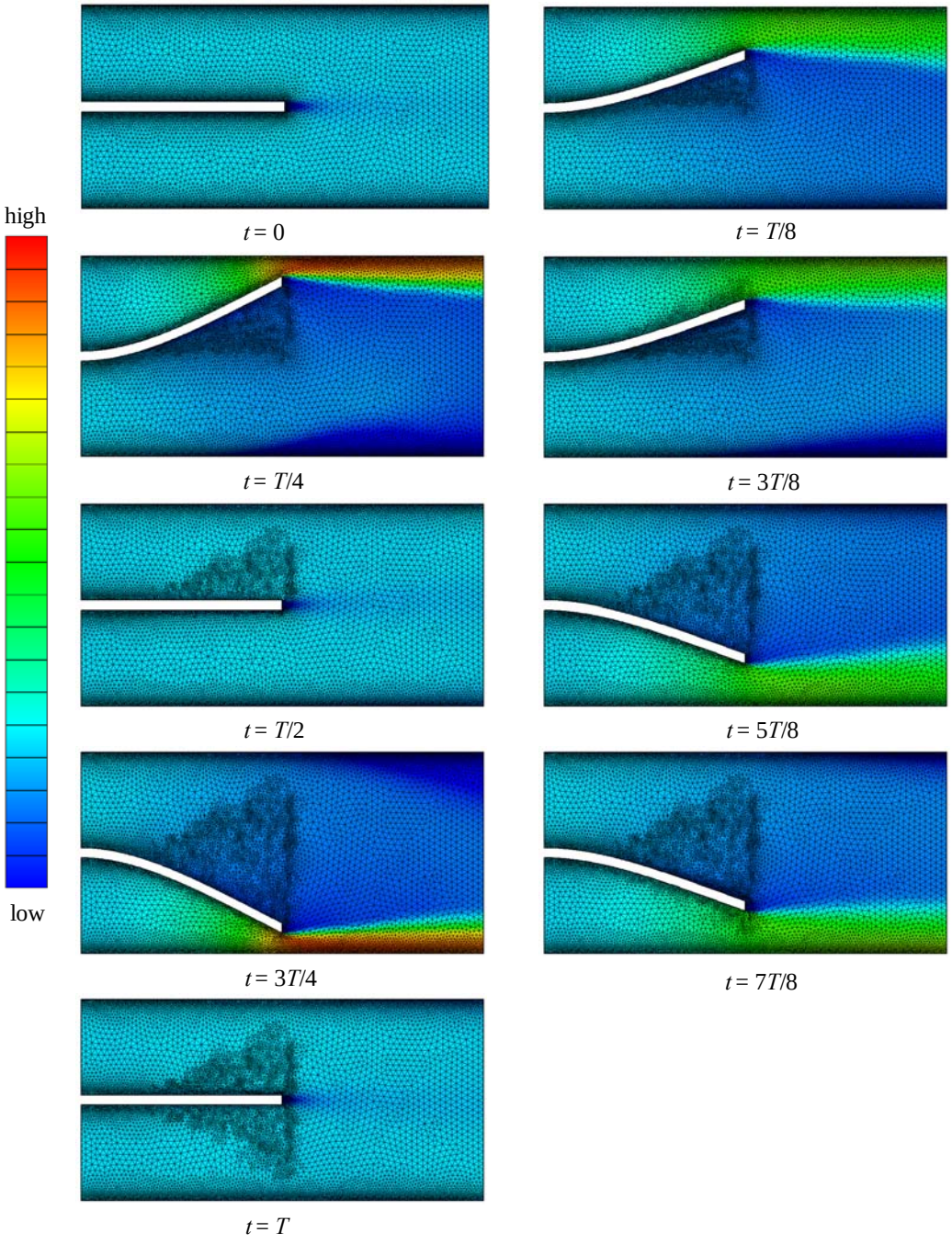

Figure 14. Velocity contours with dynamic mesh for fixed-free beam oscillating in a two-dimensional domain with uniform inflow.

In figure 15, we see that, as the ribbon moves, an area of high shear stress sweeps with it. The regions of shear stress on the bottom membrane are greatest when $\frac{T}{2} < t < T$ because the flow impinges on the bottom membrane, interacting with the ribbon, and then accelerating to the downstream opening in the filament mesh. Conversely, the regions of shear stress on the top membrane are greatest for $0 < t < \frac{T}{2}$. By comparing a time history of the shear stress and pressure drop in figure 16, we find that the oscillating ribbon has a larger influence.

Using the RNG turbulence model, we re-computed the behavior of the bending ribbon as shown in figure 17. We found that the pressure drop peaked at about 1.6 times the value for the no-ribbon case, the average shear stress about 1.25 times, and concentration ratio by 1 percent. Because we are assuming a quasi-steady analysis, the actual dynamic response of the static pressure and shear stress, considering the reduced frequency and the various phases of the ensemble of ribbons throughout the entire mesh spacer, will be considerably less as discussed below in section 4.5.

4.5 Flutter

For our proposed design to succeed, sufficient vibration of the moving member inside the mesh spacer must be maintained so that the potential for fouling is reduced by the ensuing motion. While a simulation of the coupled fluid-structure interaction would be invaluable, it is substantially beyond the scope of this study. In this section, we briefly review the characteristics of flutter and present heuristic arguments that support further examination of the concept. Ultimately, an experiment must be conducted.

Flutter, a fairly broad term applied to a class of aeroelastic phenomena affecting lifting surfaces, was first experienced prior to the Wright brothers' historic flight in 1903 and now is a fundamental criterion for licensing new aircraft designs (Blevins, 1994). An analogous term used by civil and mechanical engineers to describe the one-degree-of-freedom instability of ice-coated cables is *galloping*. Flutter occurs in two general forms:

- Static divergence
  Large steady deflections can occur if the structure does not have sufficient torsional stiffness.

- Stall flutter
  Stall is triggered by a disturbance. Dynamic plunge motions and/or torsional displacements result, and these can be coupled.

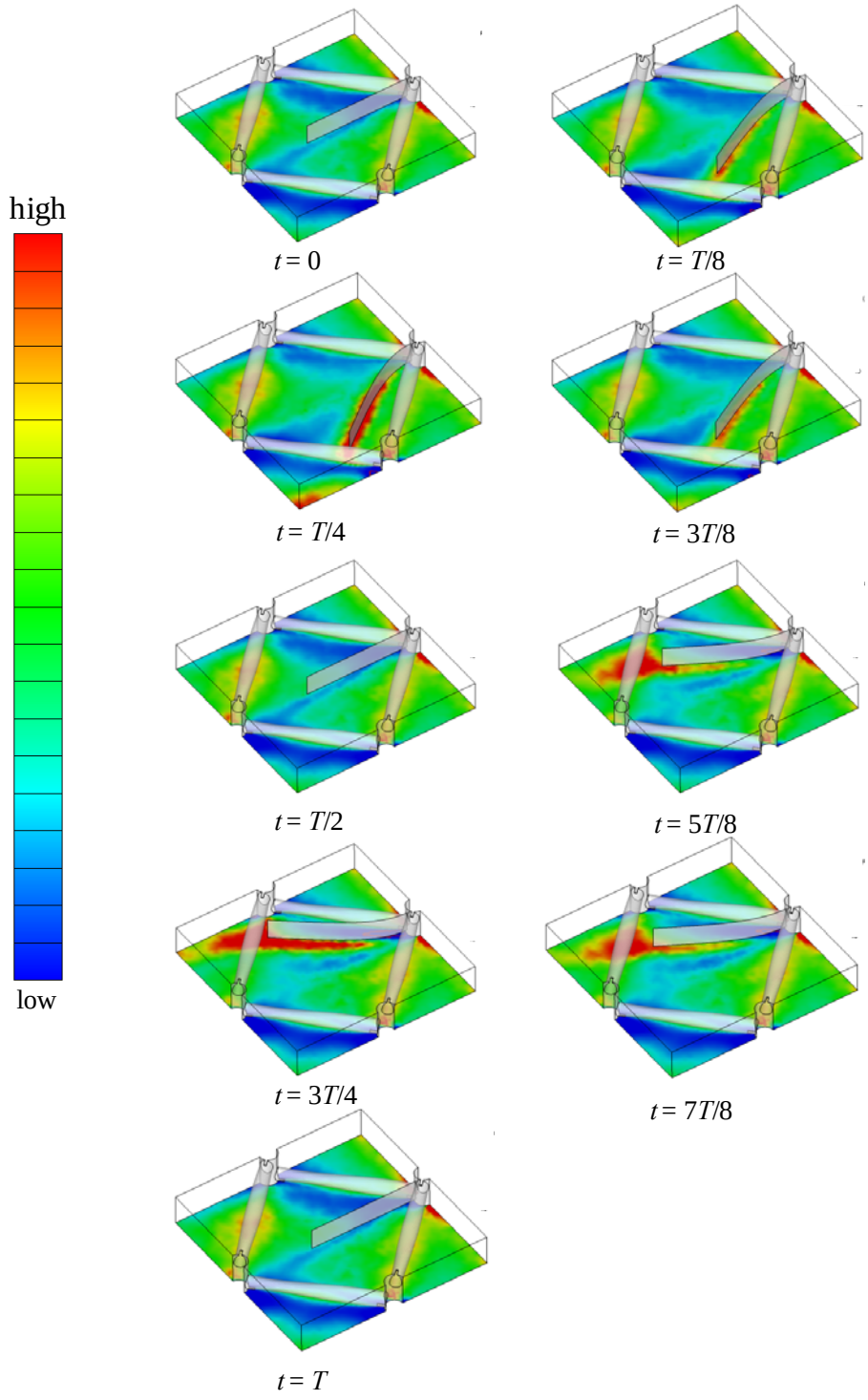

Figure 15. Shear stress contours with dynamic mesh for a zero-thickness ribbon oscillating in a three-dimensional domain with a uniform inflow.

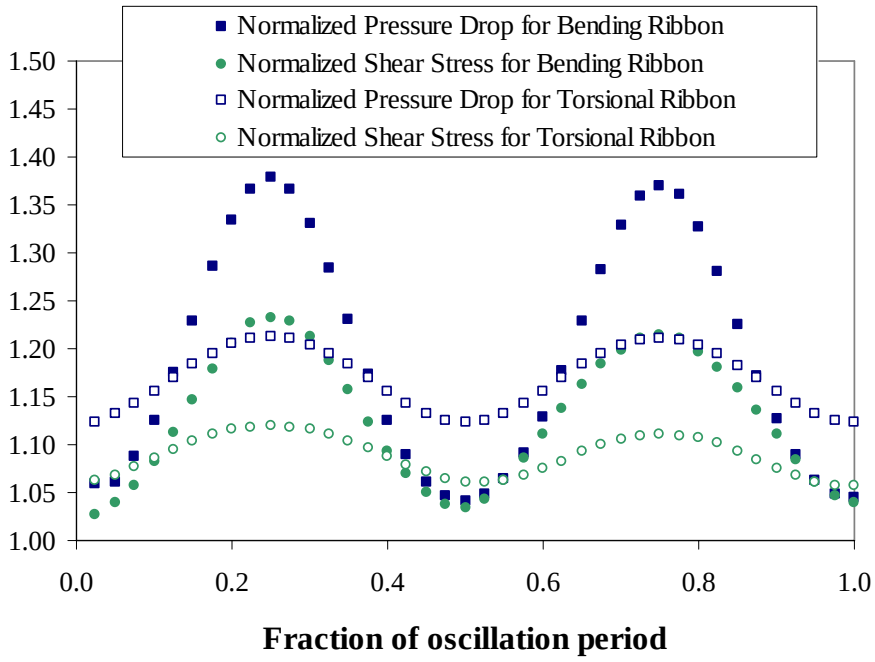

Figure 16. Pressure and membrane shear stress over one cycle of oscillation with laminar simulation.

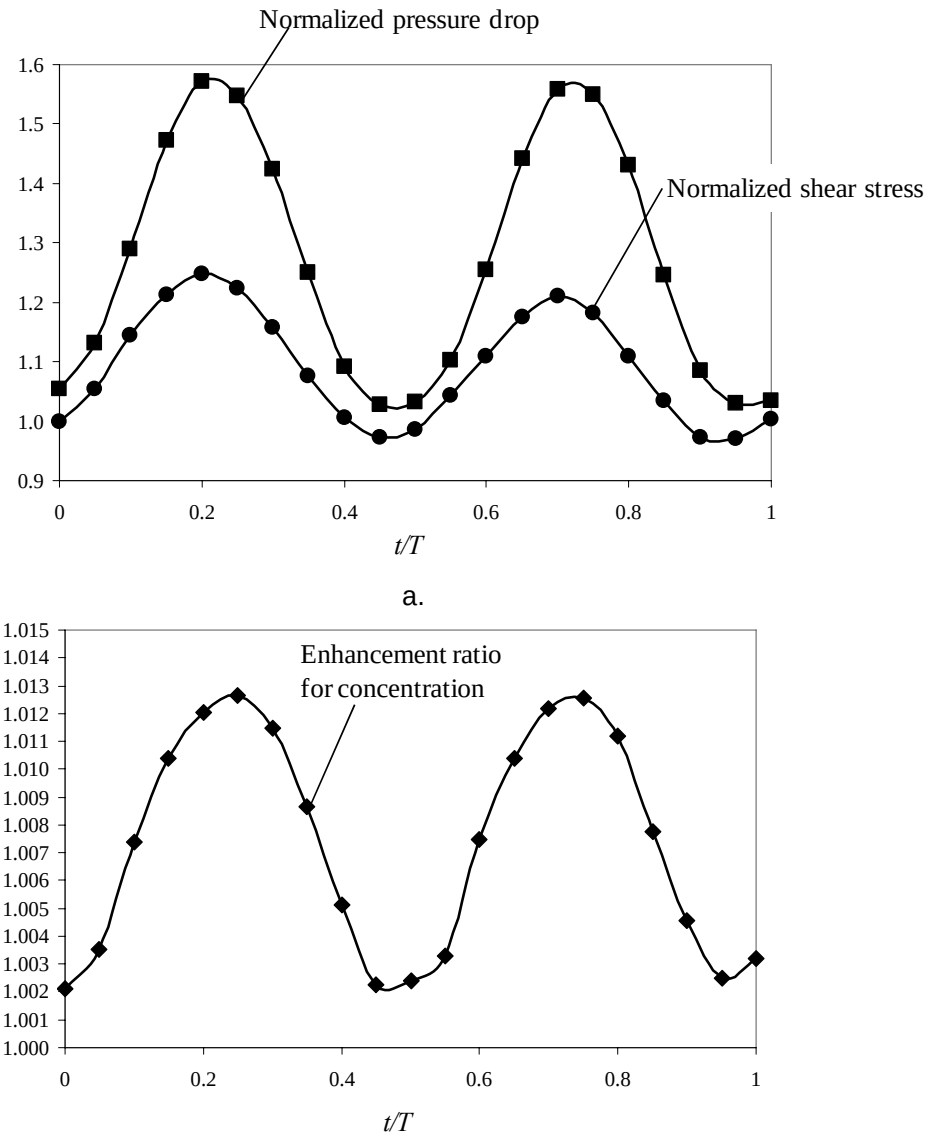

Figure 17. Behavior of synamic cantilevered ribbon over one cycle of oscillation with turbulent simulation: (a.) pressure drop and shear stress and (b.) enhancement of salt concentration.

Flutter occurs not only on wings in external aerodynamics but on the blades of turbomachinery with internal flows. The interaction of wakes from multiple blade rows and other components can dramatically affect the boundary layer, causing it to alternate between laminar and turbulent and create random pressure fluctuations through turbulence. Flutter can exist when the unsteady work on the blades exceeds the work dissipated by friction and material damping. Flutter can occur on the blades when the blade boundary layer separates.

The level of unsteadiness depends on two time scales. First, the time scale associated with the angular frequency of the unsteady motion is $\frac{1}{\omega}$. The scale associated with the time it takes a fluid parcel to travel through a cell of the mesh spacer is $\frac{\ell}{V}$. The ratio of these time scales is the reduced frequency

$$\omega_r = \frac{\omega \ell}{V} \tag{31}$$

For a reduced frequency less than one, we refer to the unsteady flow as *quasi-steady*; that is, the flow is a function only of the instantaneous conditions and not of previous conditions. For a reduced frequency much greater than one, the flow behaves in an unsteady manner and shows no quasi-steady effects.

We can calculate the unsteady forces by computing the steady forces at each instant of time. One of the oldest methods for computing the unsteady forces and moments involves the modeling of lifting surfaces with singularities and letting the singularities induce a potential flow around the blade. Theodorsen (1935) derived the exact solution for a flat plate in sinusoidally oscillatory motion. Later, Sears (1941) represented an airfoil as a flat plate of zero thickness with a continuous vortex distribution along its chord and developed an equation for the unsteady lift per unit span:

$$\tilde{L} = \frac{1}{2}\frac{d\,\mathrm{C_L}}{d\alpha}\rho \ell V \tilde{v}\,\mathrm{S}(\omega_r) \tag{32}$$

where the Sears function is

$$\mathrm{S}(\alpha_r) = \mathrm{C}(\alpha_r)\left[\mathrm{J_o}(\alpha_r) - i\,\mathrm{J_1}(\alpha_r)\right] + i\,\mathrm{J_1}(\alpha_r) \tag{33}$$

and the Theodorsen function is

$$\mathrm{C}(\omega_r) = \frac{\mathrm{J_1}(\alpha_r) - i\mathrm{Y_1}(\alpha_r)}{\mathrm{J_1}(\omega_r) - i\mathrm{Y_1}(\omega_r) + i\left[\mathrm{J_0}(\omega_r) - i\mathrm{Y_0}(\omega_r)\right]} \tag{34}$$

Both functions are plotted on the complex plane in figure 18. For a small reduced frequency, $S(a_r)$ lies near the real axis, giving a small phase angle and illustrating the validity of a quasi-steady approach. For increasing ω_r, the response is reduced and has a significant phase angle.

Note that these singularity techniques were developed for isolated thin lifting surfaces of infinite span. In the mesh spacer, the low Reynolds number infers an important role for viscous forces so that potential models may be severely limited. A coupled, fluid-structure interaction is required to properly simulate the response of the filament.

Stability to flutter, or to galloping, can be affected by the structural contour, the product of the mass and stiffness, and the damping. If the slope of the aero-dynamic force coefficient versus angle-of-attack is stable, than a bluff structure is stable. The critical velocity for the onset of galloping and flutter increases with the square root of both stiffness and mass, other parameters being equal,

$$V_{critical} \propto m^{\frac{1}{2}} k^{\frac{1}{2}} \tag{35}$$

Thus, reducing the stiffness or the mass reduces the stability. A thinner structure, for example, will have a lower critical velocity. The critical velocity for the onset of flutter is a minimum when the uncoupled natural frequencies of the torsional and plunge motions are equal (Blevins, 1994).

Similar to the desired motion of the ribbon in the center of the mesh spacer (figure 13(a)), ribbons hanging in a vertical air stream experience flutter when the flow velocity reaches a certain value—the critical velocity. Using equations of motion corresponding to hanging fluid-conveying pipes, Lemaitre et al. (2005) computed critical velocities for vertical hanging ribbons that were in reasonable agreement with his experiments. He concluded that friction instead of gravity is the dominant tensioning force in horizontal configurations. Moreover, he noted that the critical velocity of lower aspect ratio (length over width) horizontal ribbons always depends on the length, in contrast to the vertically hanging ribbons, where a sufficiently long ribbon renders the critical velocity independent of the length.

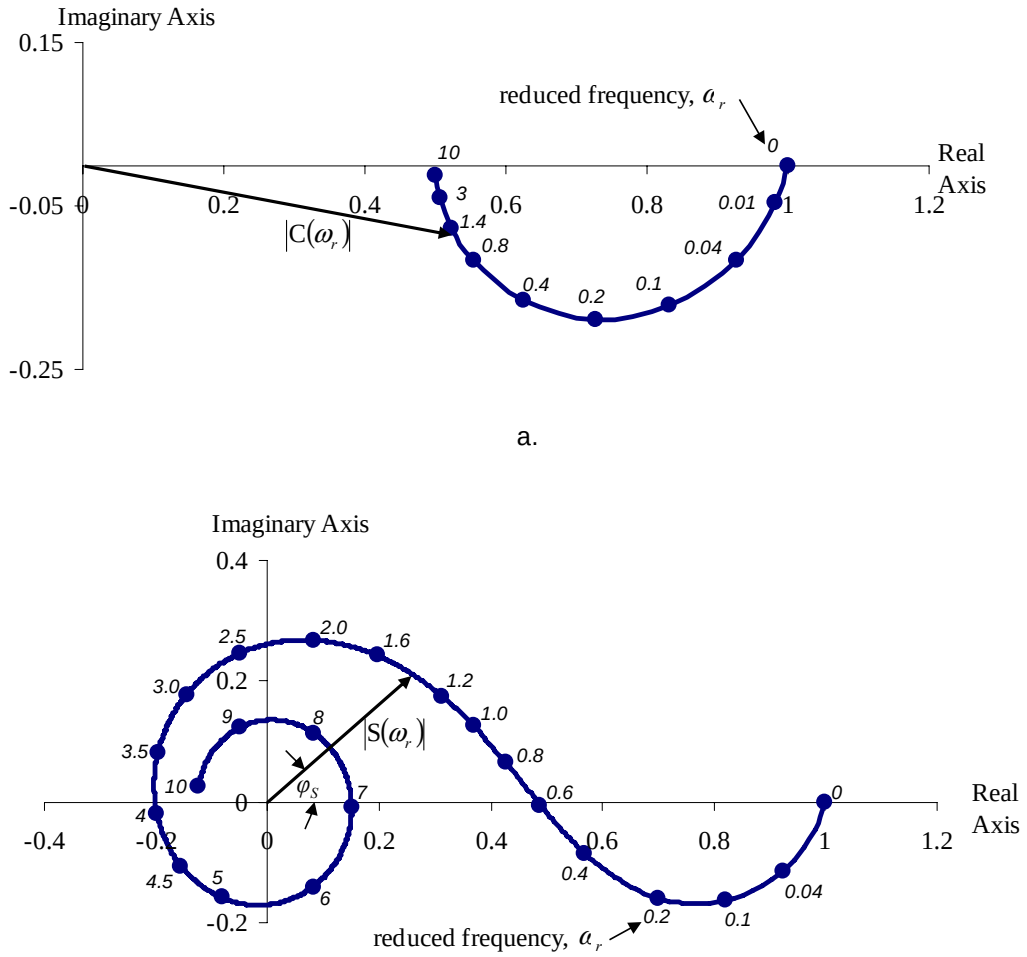

Figure 18. Aerodynamic response functions of (a.) Theodorsen and (b.) Sears.

Watanabe, Suzuki, et al. (2002) conducted an experimental study of paper flutter. Flutter speed was measured in wind tunnel tests for sheet paper and web paper of different materials, sizes, and tensions. The relationship among flutter speed, rigidity,[3] mass ratio, and tension was derived from data. The influential factors are the stiffness ratio, $\frac{EI_b}{\rho c_\ell^3}$, the tension parameter, $\frac{T_e d^2}{EI_b}$, and the mass ratio, $\frac{m}{\rho c_\ell}$, where E is the modulus of elasticity, I_b is the second moment of the area per

[3] The rigidity is given by the product of the modulus of flexural modulus, E, and the second moment of the cross-sectional area per unit length, I_b.

unit width, m is the mass per unit area, ρ is the fluid density, c_ℓ is the chord length, T_e is the tension, and d is the span length. The critical flutter speed decreases for increasing chord length and decreasing rigidity, EI_b. The dimensionless flutter speed versus mass ratio for sheet paper is illustrated in figure 19. Watanabe et al. also investigated the flutter of web paper, which is common for the production of newsprint and envelopes.

In the corresponding analytical study, Watanabe, Isogai, et al. (2002) used a time-marching Navier-Stokes simulation on a supercomputer and a potential-flow analysis on a personal computer with remarkably similar results. A parametric study was carried out with the potential flow approach, and the relationship between the mass ratio and the flutter mode was identified as shown in figure 19.

Dimensions and material properties relevant to a polypropylene ribbon with a 1-micron thickness and 0.1-inch chord yield a mass ratio, $\frac{m}{\rho c}$, of 3.2(10^{-4}), and a stiffness ratio, $\frac{EI_b}{\rho c^3}$, of 4.7(10^{-6}) m^2 per m^2. The critical velocity for flutter from Watanabe, Suzuki, et al.'s (2002) analysis is of the order of 10 m/s with large uncertainty because of the substantial extrapolation beyond the measured range. It appears likely that the cantilevered ribbon would flutter in a higher mode. The potential exists, then, for a greater coverage area for the shear stress fluctuations as shown in figure 20. The critical velocity can be lowered by using thinner materials, lengthening the ribbon, or choosing a material for the ribbon that is denser or less stiff. Behymer and Scholten (1985) report on an economical method for making polypropylene film as thin as 100 angstroms. Mesh spacers are typically constructed of polypropylene, polyester, or polyethylene.

Yamaguchi, Sekiguchi, et al. (2000) addressed flutter limits of thin sheets with both experimental measurements and an analytical approach described in a companion paper in the same journal by Yamaguchi, Yokota, and Tsujimoto (2000). They correlated four dimensionless parameters:

- The mass parameter, $\frac{m}{\rho c_\ell}$
- A flutter-limit stiffness parameter, $'' = \frac{EI_b}{\frac{1}{2}\Im V_s^2 c_\ell^3}$
- A flutter-limit reduced frequency, $f_R = \frac{fc_\ell}{V_s}$
- Surface friction coefficient, C_f

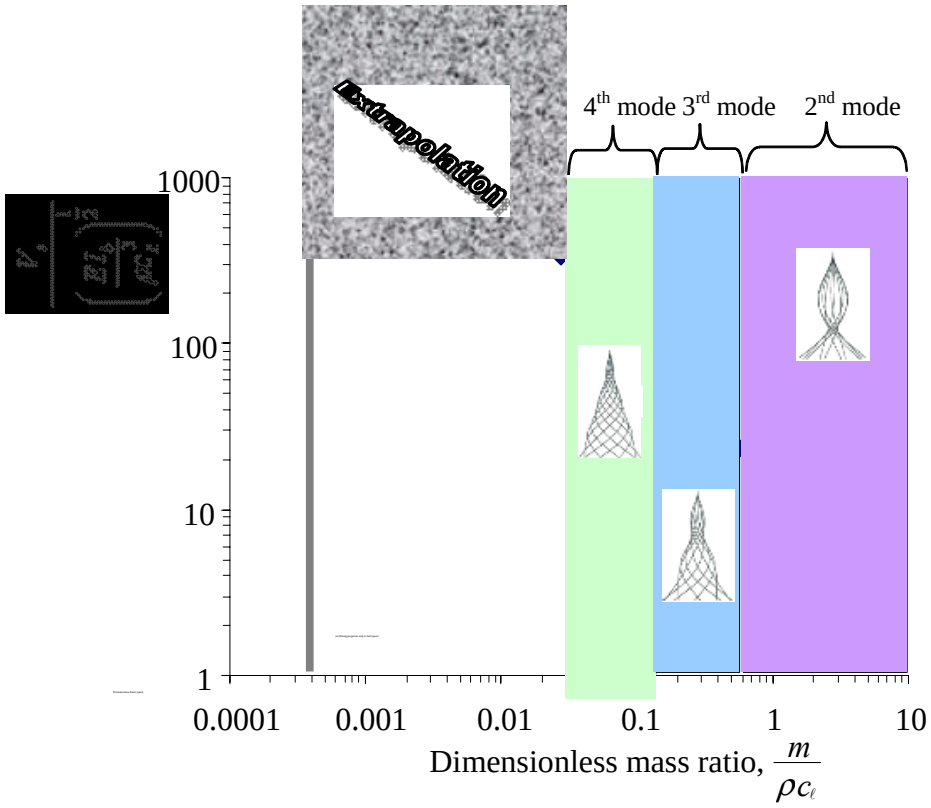

Figure 19. Dimensionless flutter speed versus dimensionless mass ratio (data from Y. Watanbe, S. Suzuki, et al., 2002).

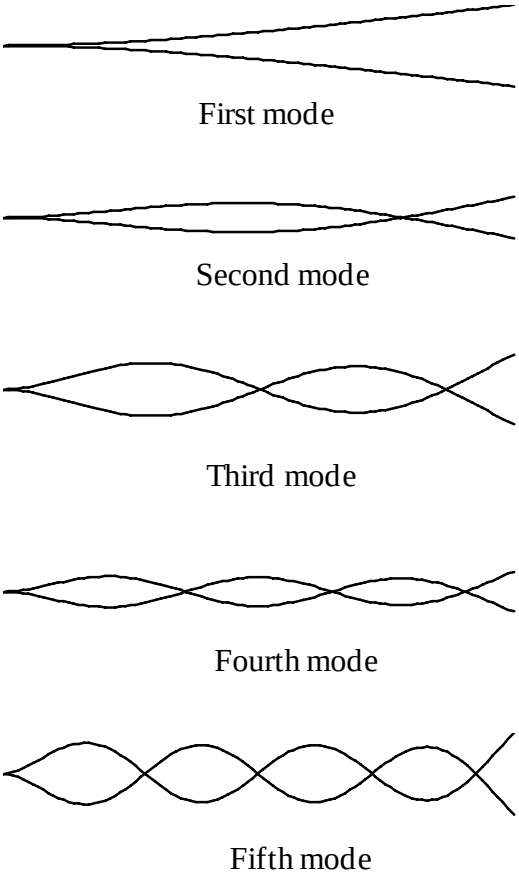

Figure 20. Mode shapes for the cantilevered ribbon.

The analytical results showed good agreement with the measured data taken for strips of various materials, thicknesses, lengths, and widths. Because air was the working fluid, the range of mass parameter reported for their data was not sufficiently low to capture the value of order 10^{-4} reported earlier for our proposed ribbon in the mesh spacer; thus, we must rely on extrapolation. For $\frac{m}{\rho c_\ell} = 3.2\left(10^{-4}\right)$, Yamaguchi et al.'s data projects a flutter-limit stiffness parameter, $\beta \approx 3\left(10^{-4}\right)$, and a flutter limit reduced frequency, $f_R \approx 1.5$. The dimensional critical velocity is in the range of the calculated crossflow velocity of 0.2 m/s. With the Sears function presented earlier as a guide, the reduced frequency indicates that the actual time response of the ribbon will be diminished in magnitude by about 70 percent and lag in phase by about 45 degrees compared to our quasi-steady analysis.

Clearly, at this juncture, we cannot establish unequivocally that flutter can be induced on the ribbon in the mesh spacer; but we believe that a flutter response

can be achieved with judicious selection of geometry and materials. As stated earlier, a simulation of the coupled fluid-structure interaction is required to determine the actual response of the ribbon, but such a project is beyond the scope of this investigation. In our simulations, we prescribed the motion of the ribbon *a priori*. While a coupled fluid-structure simulation would provide more confidence in the success of our proposed idea, ultimately, an experiment must be performed to demonstrate the concept.

5. References

Al-Ahmad, M. and F.A. Aleem, 1994. "Scale formation and fouling problems and their predicted reflection on the performance of desalination plants in Saudi Arabia," in *Desalination 96*, pp. 409-419.

Al-Bastaki, N.M. and A. Abbas, 2000. "Predicting the Performance of RO Membranes," in *Desalination 132*, pp. 181–187.

American Water Works Association, 2004. *Water Desalting Planning Guide for Water Utilities*, Water Desalting Committee, John Wiley, Hoboken, New Jersey.

Barger, M. and R.P. Carnahan, 1991. "Fouling prediction in reverse osmosis processes," in *Desalination and Water Re-use, Proceedings of the Twelfth International Symposium, Volume 3: Fouling and Scaling – Evaporative and RO Water Treatment, Synthesis and Characteristics of Membranes*, M. Balaban, ed., Hemisphere, New York.

Behymer, R.D. and J.A. Scholten, 1985. *Method for making thin polypropylene film*, Lawrence Livermore National Laboratory, Department of Energy contract report W-7405-ENG-48.

Blevins, R D., 1994. *Flow-Induced Vibration*, 2nd edition, Kreiger Publishing, Malabar, Florida.

Bureau of Reclamation, 2003. *Desalination and Water Purification Research and Development Report No. 101*, Bureau of Reclamation, Denver, Colorado, June 2003.

Buros, O.K., n.d. *The ABC's of Desalting, International Desalination Association*, 2nd edition.

Cao, Z., A. Fane, and D. Wiley, 2001. "CFD simulations of net-type turbulence promoters in a narrow channel," in *Journal of Membrane Science* 185(2), pp. 157–175.

Da Costa, A. and A. Fane, 1994. "Net-type spacers: effect of configuration on fluid flow path and ultrafiltration flux," in *Industrial and Engineering Chemistry Research* 33(7), pp. 1845–1851.

FILMTEC™, 2004. *Reverse Osmosis Membranes, Dow Liquid Separations*, Dow Chemical Company, Midland, Michigan, January 2004.

Geraldes, V., V. Semião, and M. Norberta de Pinho, 2002. "The effect of the ladder-type spacers configuration in NF spiral-wound modules on the concentration boundary layers disruption," in *Desalination* 146(103), pp. 187–194.

GWI Desal Data, 2006. 19th International Desalination Association Worldwide Desalting Plants Inventory.

Hairston, D., 2004. "Desalting process water," in *Chemical Engineering*, November 2004.

Johnson, J., 2005. Spiral-wound element with improved feed space, United States Patent 6,881,336, April 19, 2005.

Kremen, S., 1977. "Technology and engineering of ROGA spiral-wound reverse osmosis membrane modules," chapter 17 in *Reverse Osmosis and Synthetic Membranes, Theory—Technology—Engineering*, ed., S. Sourirajan, National Research Council Canada, Ottawa.

Lemaitre, C., P. Hémon, and E. de Langre, 2005. "Instability of a long ribbon hanging in axial air flow," in *Journal of Fluids and Structures* 20, pp. 213–925.

McIlvaine Company, 2007. Sales of Filtration Membranes and Equipment to Reach $11 Billion in 2011, www.wateronline.com/content/news/article.asp?docid={37d113d5e-4853-4de8c-a902-68e3789d6dad.

Pervov, A.G., 1991. "Scale formation prognosis and cleaning procedure schedules in reverse osmosis systems operation," in *Desalination* 83, pp. 77–118.

Schwinge, J., D. Wiley, and A. Fane, 2004. "Novel spacer design improves observed flux," in *Journal of Membrane Science* 299, pp. 53– 61.

Schwinge, J., D. Wiley, and D. Fletcher, 2002a. "A CFD study of unsteady flow in narrow spacer-filled channels for spiral-wound membrane modules," in *Desalination* 146(1-3), pp. 195–201.

Schwinge, J., D. Wiley, and D. Fletcher,2002b. "Simulation of the flow round spacer filaments between narrow channel walls. 1. hydrodynamics," in *Ind. Eng. Chem. Res.* 41, pp. 2977–2987.

Schwinge, J., D. Wiley, and D. Fletcher, 2002c. "Simulation of the flow round spacer filaments between narrow channel walls. 2. mass transfer enhancement," in *Ind. Eng. Chem. Res.* 41, 4879–4888.

Sears, W. R., 1941. "Some aspects of non-stationary airfoil theory," in *Journal of Aeronautical Sciences* 8, pp. 104–108.

Theodorsen, T., 1935. *General theory of aerodynamic instability and the mechanism of flutter*, NACA Technical Report No. 496.

Watanabe, Y., K. Isogai, S. Suzuki, and M. Sugihara, 2002. "A theoretical study of paper flutter," in *Journal of Fluids and Structures* 16(4), pp. 543–560.

Watanabe, Y., S. Suzuki, M. Sugihara, and Y. Sueoka, 2002. "An experimental study of paper flutter," in *Journal of Fluids and Structures* 16(4), pp. 529–542.

Yamaguchi, N., K. Yokata, and Y. Tusjimoto, 2000. "Flutter limits and behaviors of a flexible thin sheet in high-speed flow—i: analytical method for prediction of the sheet behavior," in *Journal of Fluids Engineering* 122(2), pp. 65–73.

Yamaguchi, N., T. Sekiguchi, K. Yokota, and Y. Tsuhimoto, 2000. "Flutter limits and behavior of a flexible thin sheet in high-speed flow—ii: experimental results and predicted behaviors for loss mass ratios," in *Journal of Fluids Engineering* 122(2), 74–83.

Zhang, Zh.-X., A.R. Greenberg, W.B. Krantz, and G.-Y. Chai, 2003. "Chapter 4, Study of membrane fouling and cleaning in spiral-wound modules using ultrasonic time-domain reflectometry," in *New Insights into Membrane Science and Technology: Polymeric and Biofunctional Membranes*, ed. D. Bhattacharyya and D.A. Butterfield, Elsevier, Amsterdam, pp. 65–88.